COMPUTATIONAL STUDY ON THE EFFECT OF THE MICROSTRUCTURE ON MACROSCOPIC PROPERTIES FOR CARBON FIBER FELTS

MASTER'S THESIS

Joan Baptista Rico Orero

Escola Tècnica Superior d'Enginyeria del Disseny
Universitat Politècnica de València

École polytechnique de Bruxelles
Université libre de Bruxelles

June 2020

COMPUTATIONAL STUDY ON THE EFFECT OF THE MICROSTRUCTURE ON MACROSCOPIC PROPERTIES FOR CARBON FIBER FELTS

Report on the work developed during a Short Training Programme at
the von Karman Institute for Fluid Dynamics
during the period from February to June 2020

Directed by:

Eng. Francisco Torres, thesis adviser from VKI
Dr. Alessandro Turchi, project coordinator at VKI
Prof. Dr. Thierry E. Magin, thesis supervisor at VKI
Prof. Dr. Patrick Hendrick, thesis supervisor from ULB
Prof. Dr. Eugenio Giner, thesis supervisor from UPV

Escola Tècnica Superior d'Enginyeria del Disseny
Universitat Politècnica de València

École polytechnique de Bruxelles
Université libre de Bruxelles

June 2020

Acknowledgements

Do not be afraid to ask for help. Nobody gets through college on their own.

Michelle Obama at the Beating the Odds' Summit

This work is partially supported by ESA contract no. 4000122914/18/NL/KML (AblaNTIS).

Foremost, I would like to express my sincere gratitude to you, Fran, for the continuous support on my work, for your patience, enthusiasm, and knowledge. Your guidance helped me in all the time of research and writing of this paper. Moreover, your dedication and mentoring has motivated me to rethink my career and to pursue a PhD programme; a branch I had never thought about! Et desitge molta sort per a la conclusió de la teua recerca.

Moreover, I would also like to thank Alessandro and Thierry for all the fundamental instructions without which, the development of this thesis would not have been such. Also acknowledge Joffrey Coheur for his revision.

My thanks goes also to Pr. Hendrick, for the passion showed during your lectures. I have learned as much from your answers as from your questions.

My greatest appreciation to the NASA Ames Research Center for developing and publishing PuMA as an open source, and to the HPC team for granting me the permission to use the Hydra cluster of the VUB and ULB.

Merci de tout mon coeur à ceux qui ont célébré tous mes succès comme s'ils étaient les siens et m'ont tellement aidé pendant la quarantaine. Même si on ne se revoie plus jamais, on restera toujours le skydem plus professionnel!

Gràcies a tu per fer-me pensar a cada xerrada i per fer-me veure que les coses poden ser d'una altra manera. Tant de bo haver tingut més certesa. O tant de bo no.

Last but not least, I would like to thank my family, specially my parents without whom nothing of this would have ever been possible. This time the gratitude is, if possible, even larger. Thank you for your support and your infinite kindness during these last months, and needless to say, during my whole life. Vos estime.

Abstract

Carbon/phenolic ablators are successfully used as thermal protection materials for spacecraft. Nevertheless, the characterization of their properties experimentally in a microscopic scale is expensive and time-consuming. Accurate and robust numerical models are required to optimize design margin policy. The feasibility of using numerical models to extract effective material properties of carbon/ablators is assessed. In this thesis, a synthetic model based on CALCARB® CBCF 18-2000 is developed using the Porous Microsctucture Analysis (PuMA) software. This model is first validated with available experimental data and then is applied to represent the response of carbon fibers exposed to high temperatures. The synthetic model faithfully represents the simulation of experimental analyses given a limited number of parameters. Even though further verification of the model must be done by comparing with the analysis of microtomographies from real materials, these results open the possibility for generating better carbon/phenolic ablators with the aid of computer simulations.

Keywords— carbon/phenolic ablators, thermal protection systems, porous materials, microstructure, thermal conductivity.

Contents

List of Figures

List of Tables

List of Symbols

Non-dimensional numbers

Kn	Knudsen number	$\frac{\lambda}{L}$
Ma	Mach number	$\frac{u}{a}$
Pe	Péclet number	$\frac{Lu}{D}$

Greek symbols

α	Thermal Diffusivity	$\mathrm{mm\,s^{-1}}$
α^*	Confidence level	-
ϵ	Porosity	-
θ	Plane angle	°
κ	Thermal conductivity	$\mathrm{W\,m^{-1}\,K^{-1}}$
κ_{f}	Intrinsic thermal conductivity of the fibers	$\mathrm{W\,m^{-1}\,K^{-1}}$
κ_{m}	Thermal conductivity of the medium	$\mathrm{W\,m^{-1}\,K^{-1}}$
$\bar{\lambda}$	Mean free path	m
μ	Dynamic viscosity	Pa s
ρ	Density	$\mathrm{kg\,m^{-3}}$
σ	Electrical conductivity	$\mathrm{S\,m^{-1}}$
σ^*	Standard deviation of the sample	-
τ	Tortuosity	-
ϕ	Volumetric fraction	-

Roman symbols

a	Speed of sound	$\mathrm{m\,s^{-1}}$
A	Area	$\mathrm{m^2}$
c_p	Heat capacity	$\mathrm{J\,kg^{-1}\,K^{-1}}$
d_f	Fiber's diameter	µm
D	Mass diffusivity	$\mathrm{m^2\,s^{-1}}$
k	Permeability of the medium	$\mathrm{cm\,s^{-1}}$
L	Representative physical length scale	m
l_D	Capillarity diameter	µm
l_f	Fiber's length	µm
l_v	Voxel's length	µm
N	Molar flux	$\mathrm{mol\,m^{-2}\,s^{-1}}$
p	Pressure	Pa
q	Instantaneous flow rate	$\mathrm{m^2\,s^{-1}}$
R_g	Gas constant	$\mathrm{m^2\,kg\,s^{-2}\,K^{-1}\,mol^{-1}}$
T	Temperature	K
t	Time	s
u	Flow velocity	$\mathrm{m\,s^{-1}}$
U	Voltage potential	V
$\bar{v}$	Mean thermal velocity	$\mathrm{m\,s^{-1}}$
V	Volume	$\mathrm{m^3}$
x	Distance	m
X	Domain length in X direction	-
Y	Domain length in Y direction	-
z_α	Z-score for a given α	-
Z	Domain length in Z direction	-

Acronyms

AblaNTIS	Ablative-material Numerical-Test International Series
CF	Carbon Fiber
CT	Computerized Tomography
CBCF	Carbon-bonded carbon fiber
DLR	Deutsches Zentrum für Luft- und Raumfahrt
EJFD	Explicit-Jump Finite Difference
ESA	European Space Agency
FFT	Fast Fourier Transform
FFTW	Fastest Fourier Transform in the West
FoS	Factors of Safety
GUI	Graphical User Interface
HPC	High Performance Computing
HRSI	High Temperature Surface Insulation
IUPAC	International Union of Pure and Applied Chemistry
LFA	Laser Flash Analysis
MEV	Maximal Elementary Volume
MOE	Margin of error
NASA	National Aeronautics and Space Administration
NSD	Normalized Standard Deviation
PAN	Polyacrylonitrile
PRNG	Pseudorandom Number Generation
PTFE	Polytetrafluoroethylene
PICA	Phenolic Impregnated Carbon Ablator
PuMA	Porous Microstructure Analysis
Q-Q	Quantile-Quantile
REV	Representative Elementary Volume
SA	Surface Area
SEM	Scanning Electron Microscopy
SFD	Simple Finite Difference
SSA	Specific Surface Area
TIFF	Tagged Image File Format
TPS	Thermal Protection System
ULB	Université libre de Bruxelles
UPV	Universitat Politècnica de València
VKI	von Karman Institute for Fluid Dynamics
VUB	Vrije Universiteit Brussel

Chapter 1

Introduction

Since the first steps of space exploration, reutilization of rockets and spacecraft has been a main concern for all space programs as it greatly reduces production costs. Moreover, when humans started to journey into outer space, it became mandatory in order to be able to safely return home. Nowadays, the requirements remain always valid for earth reentry but has been further extended to permit the solar system exploration.

Starting from the beginning, the atmospheric entry is the passage of an object from outer space into a planet or natural satellite through its surrounding gaseous atmosphere. These objects may enter the atmosphere in an uncontrolled way (as meteors or space debris) or in a controlled way following a designed path. Either way, these bodies reach hypersonic speeds around Mach 25 which induce high mechanical stresses due to drag forces and high thermal effects mainly due to air compression in front of the object. At these speeds, detached shock waves are created around the blunt body and may cause a rise in temperature that can even exceed 10 000 K causing loss of mass (ablation) and even complete disintegration of the object. When dealing with man-made spacecraft, it is therefore essential to protect its integrity by means of a Thermal Protection System (TPS) [1].

1.1 Thermal Protection Systems

Spacecraft were usually designed with aluminum because of its outstanding combination of lightweight, strength and workability. However, this structure cannot withstand temperatures over 448 K without structural failure [2]. Moreover, during reentry (and also in a moderate way during liftoff), surface temperatures will be pushed well above the melting point of aluminum 993 K so doubtlessly an effective insulator is required. Nevertheless, it is widely known that it does not exist any kind of material able to withstand temperatures over 5000 K. So, at this point is where the design of TPS comes into play. In fact, the TPS is a critical component of a planetary mission as it is a single point-of-failure subsystem with no back-up, so its performance needs to be faithfully validated through analyses and ground testings. However, the knowledge of these systems still requires much improvement in order to avoid issues such as the one shown at Figure 1.1, in which due to the complexities of the atmosphere of Titan, the lack of accuracy of the ablation predictions was evidenced.

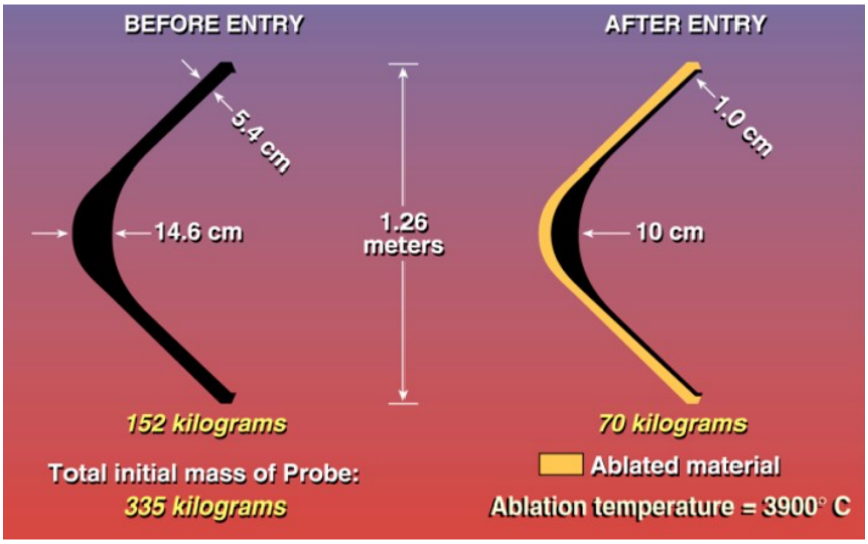

Figure 1.1: Galileo Probe Heatshield Ablation [3]. It can be seen how the remaining material in the sides of the TPS was minimal, while in the front it was clearly oversized.

Two main types of TPS have been developed for this purpose: ablative and re-usable. The first designs to be developed were the ablative heat shields. In fact, the concept of a decomposing material which would help to protect the surface of the spacecraft was described as early as 1920 by Robert Goddard [4]: "*In the case of meteors, which enter the atmosphere with speeds as high as 30 miles per second, the interior of the meteors remains cold, and the erosion is due, to a large extent, to chipping or cracking of the suddenly heated surface. For this reason, if the outer surface of the apparatus were to consist of layers of a very infusible hard substance with layers of a poor heat conductor between, the surface would not be eroded to any considerable extent.*". From this definition it can be understood quite straightforwardly how the protection is achieved. In a few words, this kind of thermal protection is produced through physico-chemical transformations and rejection of eroded material to dissipate heat. These were the systems used in the first years of the Space Race in many famous spacecrafts as the Vostok I and Apollo command modules.

Afterwards, reusable heat shields were developed in opposition to ablative TPS. In these designs, ceramic materials with high melting point and low thermal diffusivity were used to dissipate heat in terms of radiation, seeking an equilibrium between the incoming heat flux and the re-radiated energy. At first, in the early 1970s, huge research was done for a wide range of quality refractor metals based on molybdenum and molybdenum–rhenium alloys that were covered with protective coatings. However, these heavy alloys were abandoned few years later as the focus was then shifted towards ceramic reusable materials [5]. Up to now, this system has been completely implemented only on the American Space Shuttle and on the Russian Buran, which flew only once. The TPS of the Space Shuttle was made up of special silicon tiles that were placed all over the skin —up to 20548 high temperature surface insulation (HRSI) tiles—, each one of them specifically manufactured and labeled. The leading edges of the blunt body and the wings were reinforced with carbon-carbon composite material in order to withstand the aerodynamic heating due to their critical situation caused by the combination of compression and surface friction of the atmospheric gases.

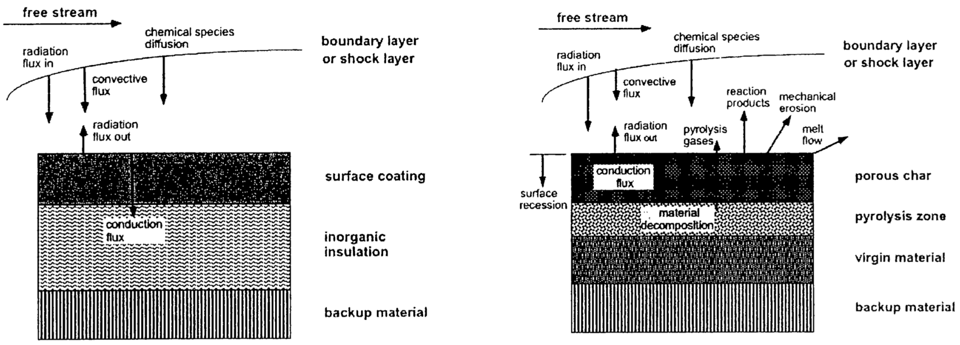

Figure 1.2: Energy accommodation of reusable (left) and ablative (right) TPS materials. [3]

While the Shuttle's TPS was very effective, several reasons caused the shift of the focus again to the ablative TPS materials. One of the main issues was the high density of these materials, in contrast with ablative TPS and their lightweight properties. Moreover, this shift was accelerated following the Columbia disaster in which due to the fail of a single HRSI tile, the spacecraft disintegrated during re-entry causing the death of its 7 crew members. All the rest of the reentry capsules (the Soyuz, the Shenzhou, etc. and even the in-test-mission SpaceX Dragon) they have implemented the ablative heat shield type.

1.2 Ablative thermal protection materials

Mainly because of these reasons, during this work the focus will be brought into ablative materials. In fact, it is clear how the interaction with the environment of the latter will be more complex as many more mechanisms are involved in the accommodation of the entry heating [3], as it can be observed in Figure 1.2. This justifies the need of extensive and precise analysis campaigns carried during the last years in order to improve these systems. Moreover, in order to allow for future space exploration, the demands for thermal shielding will go beyond the current state-of-the-art. Therefore, improved understanding of thermal protection materials is absolutely essential to improve the design and thus decrease the safety factors and ensure the feasibility of these projects [6].

This new generation of ablative materials are usually made up of composite thermal protection materials based on composed as hybrid thermal protection systems based on an organic precursor such as carbon fiber (CF) felts and a polymeric isotropic matrix. The former is usually used to provide the thermal properties. The latter, to embed the fibers and shape the material. These materials compose a structure with pyrolytic, ablative, and insulating capabilities but featuring low densities ($\sim$300 kg m^{-3}) and high porosity ($\epsilon > 0.8$). Thus, they are able to dissipate the impinging hyperthermal fluxes through a disintegration process, by transforming the received energy into chemical processes and receding physically, while the remaining virgin material is able to insulate the spacecraft. They are usually characterized by their thermal response and structural properties (such as density, heat transportation or ablation rate, among others) in both their virgin and charred states. Nowadays there exist many examples of these materials, as the Phenolic Impregnated Carbon Ablator (PICA) and AVCOAT 5026–39 (both developed in the second half of the 20th century by NASA), or Asterm and AQ61 (developed by Airbus). However, in this work the material of reference will be the ZURAM®, a material developed by DLR (Germany) for research purposes.

In a few words, the process through which an ablative material protects the spacecraft from the high thermal stresses is through its decomposition, which being an endothermic reaction, it allows to absorb large amounts of heat. The result of this process is the transformation of the solid material into a gaseous state, with the subsequent loss of mass and the recession of the surface. The decomposition process can be divided into two mechanisms: pyrolysis and ablation. The pyrolysis is the mechanism by which the resin gets degraded and carbonized; and the ablation is a group of processes which induce the removal of material from the surface [7].

The organic matrices commonly used to produce polymeric ablatives can be divided into two main groups: noncharring and charring matrices. Noncharring materials such as PTFE, completely decompose to a gaseous state without leaving solid residues at temperatures higher than 500 °C, consequently hindering the convective heat transfer from the hot plasma flow to the solid body. On the other hand, charring polymers volatilize leaving residual material. The most common materials these days are the phenolic resins as they are cheaper and easier to obtain than its substitutes, but also they have an outstanding thermal stability and they contain high amounts of carbon and low of oxygen, which limits the amount of volatiles like carbon monoxide and dioxide [8].

Summing up, the heat blockage process is carried in three ways. 1) The volatilization (pyrolysis) of the material being an endothermic reaction, it allows to absorb some amount of heat in the process. 2) During this process, hydrocarbon gases are formed and percolate through the material until reaching the external heated surface and boundary layer, causing a reduction in the heat by convection through the so-called blowing. 3) The charred carbonaceous residues commonly known as char, help protecting the virgin material below by partially re-radiating energy and by working as a thermal sink [9]. All these processes may be seen in Figure 1.2.

Studying the conductivity of these systems and of their different composing materials is fundamental, as they do not behave all in the same manner. Thermal conductivity plays a fundamental role in the aforementioned processes, and this property being too high will cause the failure of the complete system. Therefore, it is essential to thoroughly characterize the properties of both the carbon fibers and the phenolic resin to allow the development of reliable macroscopic models. As it could be seen in Figure 1.1, during the reentry of a space vehicle into the atmosphere, the amount of material lost is not negligible, and because of this reason, it is fundamental to correctly measure the recession rate of the materials used, to sufficiently protect the spacecraft.

1.3 Modeling the material thermal properties

Complementary to the experimental research, computational analyses have been typically carried over using a volume-averaged approach, with macroscopic models [10]. However, they rely on experiments or detailed simulations to determine effective transport properties such as the thermal conductivity.

Many mathematical models have been proposed to estimate the effective thermal conductivity of porous materials, by describing the influence of each phase (solid, gas) into the final value obtained. However, experimental analyses have demonstrated that these legacy models successfully represent the real characteristics for the case of materials with macro-scaled pores, but they fail regularly when the pores are micro- and nano-scaled [11].

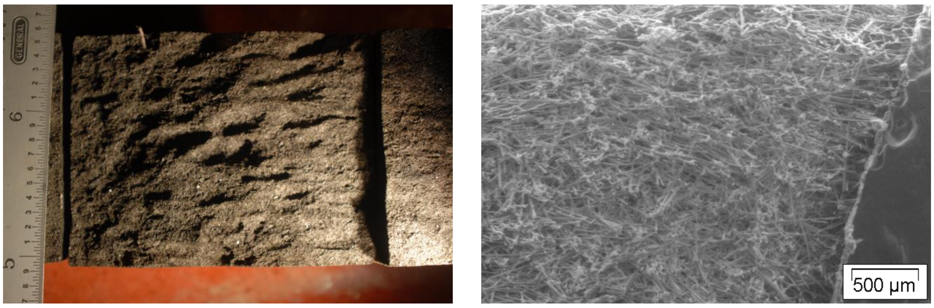

(a) $\mathcal{O}$ (cm) (b) $\mathcal{O}$ (mm)

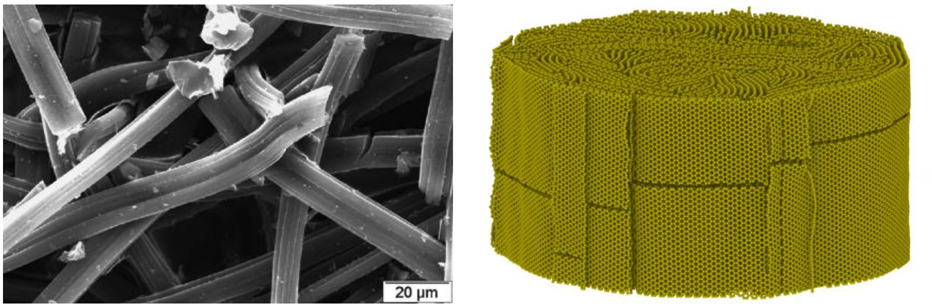

(c) $\mathcal{O}$ (μm) (d) $\mathcal{O}$ (nm)

Figure 1.3: Range of scales for the different approaches [12]. From macroscale (Fig. 1.3a) to nanoscale (Fig. 1.3d).

Experimental methods have been developed to measure the effective conductivity, but they are usually expensive in resources and time. Moreover, there are other properties, such as tortuosity, which cannot be measured with low uncertainty. Therefore, nowadays, other methodologies are followed.

A multi-scale approach (Fig. 1.3) is designed in order to fully represent all the processes occurring in the material. While the experimental and macroscopic analyses still remain used, microscopical analyses are developed to complement the volume-averaged approaches with an analysis which takes into account the real properties of the micro-geometry and allow for the interpretation of experimental data. This step is fundamental in the correct development of the whole approach, as it allows to faithfully represent real properties with scant resources. This is important when simulating oxidation reactions of highly porous ablators (Fig. 1.4), where percolation processes may take place and cause different behaviors in oxidation phenomena, but also to define intrinsic properties of the materials. Moreover, further in-depth analyses are usually carried out to fully understand the molecular dynamics at a nano-scale order.

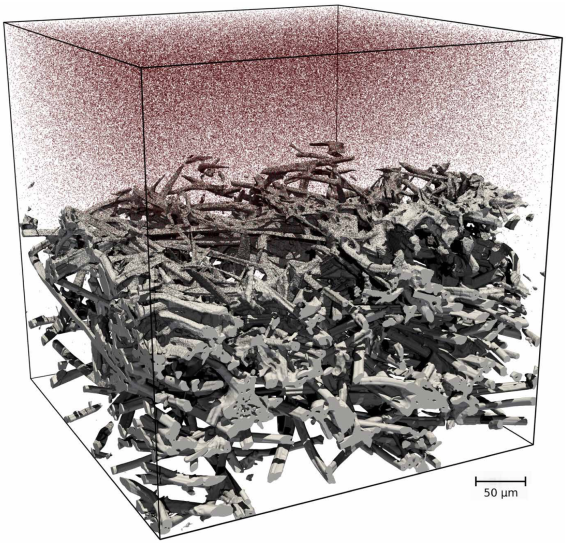

Figure 1.4: Microscale ablation simulation of an oxidizing heat shield. [13]

At microscale, modern imaging devices are capable of producing large three-dimensional data sets representing material structure with resolution lower than 1 µm. Naturally, an interest arises in computing properties based on these capabilities. These imaging techniques segment the volume into regions with constant grey values and reinterpret them to represent solid cubic cells (called voxels) with constant properties determined by the greyscale [14]. With this technique is possible to perform computations over a numerical model that perfectly represents the microgeometry of porous materials, in order to measure properties which are otherwise beyond reach.

1.4 Objectives and outline

In the following study all the analyses are framed into the microscale modeling. Thus, imaging is simulated by using simplified digital models that describe the statistical three-dimensional morphology of ablative materials, allowing their characterization. To do so, the Porous Material Analysis (PuMA) software, developed at NASA Ames Research Center, is used to compute material properties from microstructures.

The main objective of this thesis is to develop a methodology to reproduce the behavior of macroscopic properties of porous materials, based on tools which simulate their microstructure. More specifically, three objectives are identified:

- Develop a synthetic model and evaluate the influence of the properties of interest on macroscopic properties.

- Validate the created model through its comparison with experimental data.

- Reproduce and study the microscopic effects measured through LFA on carbon fiber materials when exposed to high temperatures.

To achieve this, first, a parametric study is carried out on an artificially-generated model which resembles the characteristics of typical carbon fiber preforms to get familiarized with porous materials. Then, a numerical model of a commercial carbon fiber preform is developed and compared to experimental data. Finally, a study is carried out to better understand the response of carbon fiber preforms when exposed to high temperatures. This is performed by a partial reproduction of literature measurements of thermal conductivity at different conditions.

The project is structured as follows:

- In **Chapter 1** an introduction to the space exploration and thermal protection systems is given.
- In **Chapter 2** a specific literature review is performed to understand the physical properties and phenomena involving porous materials.
- **Chapter 3** is devoted to the explanation of how properties are computed in PuMA and to offer a user guide explanation of the software.
- During **Chapter 4** a synthetic model is generated based on CALCARB® CBCF 18-2000, and a study on the influence of the properties of interest is carried out.
- In **Chapter 5**, the model previously generated is validated with experimental data and is then used to help in the comprehension of results obtained through LFA.
- **Chapter 6** summarizes the different results obtained through the development of the thesis and presents foreseen future work.

Chapter 2

Porous materials and lightweight ablators

As it has been previously presented in Chapter 1 this study focuses on the investigation of thermal properties of carbon/phenolic ablative TPS materials. Thus, a brief review on physics of porous media, particularities of carbon/phenolic ablators and a small review on experimental characterization methods is presented in the following.

2.1 Physical aspects of porous materials

Historically, porous materials have been studied by a volume-averaged approach based on Darcy's law thus, assuming the porous structure as a whole solid unit with global characteristics. This law is experimentally based in order to describe fluid movements through a porous media and is stated as:

$$q = -\frac{K}{\mu}\nabla p \tag{2.1}$$

being q the flow rate, K the permeability of the medium, μ the dynamic viscosity and ∇p the pressure loss over the characteristic length.

However, Darcy's law is only valid in a continuum homogeneous viscous flow where inertial forces are negligible, with Reynolds numbers lower than 1, which may be recreated in experimental analyses but do not resemble at all atmospheric entry conditions.

Nevertheless, there exists a correction for gas flow in domains with very small characteristic length, also known as Knudsen diffusion. This kind of diffusion occurs when the scale length of a system is comparable to or smaller than the mean free path[1] of the particles involved, as in these cases, interactions wall-particle occur with further assiduousness and resulting in additional wall friction. For this case, the equation might be written as in Equation (2.2), where N is the molar flux, R_g is the gas constant and $D_\mathrm{K}^\mathrm{eff}$ is the effective Knudsen diffusivity of the porous media [15].

$$N = -\left(\frac{k}{\mu}\frac{p_\mathrm{a}+p_\mathrm{b}}{2} + D_\mathrm{K}^\mathrm{eff}\right)\frac{1}{R_\mathrm{g}T}\frac{p_b - p_a}{L} \tag{2.2}$$

A good reference for the relevance of the Knudsen diffusivity is the Knudsen number (Eq. (2.3)). This nondimensional number indicates if the continuum assumption is valid. If the Knudsen number is in the order of magnitude 0.01 or lower, it might be approximated to a continuum flow. However, if the ratio between the mean free path of a molecule and the length scale of the problem is higher than 10, then such assumption is not valid anymore and it is usually assumed to be in presence of rarefied flow [16]. Therefore, a Knudsen number greater than one indicates Knudsen diffusion is important and Eq. (2.2) should apply.

$$\mathrm{Kn} = \frac{\bar{\lambda}}{L} \tag{2.3}$$

where $\overline{\lambda}$) is the mean free path and L the representative physical length scale. Usually in the kind of problems similar to the ones addressed in this study, the characteristic length is defined by the capillarity diameter (theoretical size of the pores in the domain) and represented by l_D.

When simulating the oxidation reactions of highly porous ablators, it is fundamental to take another approach to correctly analyze the oxidation phenomena at a microscopic scale in order to fully understand the effects of diffusion mass transport and gas-surface reactions. Nowadays, with improved computational capabilities, it is possible to characterize these processes and faithfully representing the geometries through the import of digitalized microstructures.

2.1.1 Porosity

Porosity ϵ (or volume fraction ϕ of the void phase) is the void space proportion in the total volume of a material. Both absolute and relative porosity may be addressed depending on how it is measured. The former is the most typical one and takes into account all the void parts of the material. The latter, however, just measures the void volume which is accessible from the exterior, so for instance, if the fibers of the material are hollow, that would not be added into the computations.

---

[1] Mean free path: Medium length of a path traveled by a moving particle between successive collisions which modify its direction.

The porosity is usually calculated as the ratio of the apparent volume V_p of the sample, which is attributed to the pores or void space, with respect to the complete volume of the body [17]:

$$\epsilon = \frac{V_p}{V}. \tag{2.4}$$

Another way of calculating it is from the bulk density ρ_{bulk}, the saturating fluid density ρ_{fluid} and particle density ρ_{particle} using:

$$\epsilon = \frac{\rho_{\text{solid}} - \rho_{\text{bulk}}}{\rho_{\text{solid}} - \rho_{\text{fluid}}}. \tag{2.5}$$

When referring to microporosity, small defects in the fibers of the material are discussed and usually they are smaller than 2 nm in diameter as defined by the IUPAC [18]. This type of porosity will not be treated here.

Porosity is a fundamental property for ablative carbon/phenolic materials. Its value range must be such that, it is high enough to let the gaseous phase of the resin percolate through the material but low enough to trap it inside and increase inner pressure, as explained in Chapter 1.

2.1.2 Surface area and specific surface area

The surface area of a porous material is defined differently than for non-porous ones. For porous material, it is the sum of the area for each of the fibers considered in the domain, therefore, it is usually much lower than the external surface area of the domain, and it depends on parameters such as the radius of the fibers or the shape of the fibers precision of the measurements Form it, the specific surface area may be defined as the ratio between the surface area and the complete volume of the sample. It is expressed in m^{-1}.

When digitalizing real materials, the main issue comes from creating a correct rendering of a surface which may be able to correctly separate the voxels that are part of the object from those which are not. Several methods have been developed with this purpose, the Cuberilles and the Marching Cubes methods are the most common ones [19].

The Marching Cubes Algorithm was developed by Lorensen and Cline [20] and it is based on the division of the input volume into a discrete set of cubes and therefore creating triangular models of constant density surfaces. Those triangles are computed first by importing the model with a gray-scale vertex sampling and assigning to each voxel its corresponding active vertices. Then, as each of the vertices may or may not be part of the geometry, 2^8 different arrangements arise possible, but they may be encapsulated into just 15 families (as shown in Fig. 2.1) which allow to obtain all the different combinations with rigid rotational matrices.

It seems straightforward that as the discretization of the geometry increases, the obtained result will represent more accurately the real sample. However, the Marching Cubes Algorithm was verified by Ferguson et al. [21] against the Cuberille method, in order to check the adjustment of them both to the specific problem. In the latter, a similar approach to the modeling of the geometries is followed, with the difference that instead of creating isosurfaces inside each voxel, complete cubes are represented as it may be perceived at the sketch of Figure 2.2 designed by Nielson [22].

The results of this comparison concluded a great increase on the representation reliability for the Marching Cubes Algorithm, as its error percentage converged to values of the order of the 10% while for the Cuberilles one, errors were expected to nudge a 50 % error.

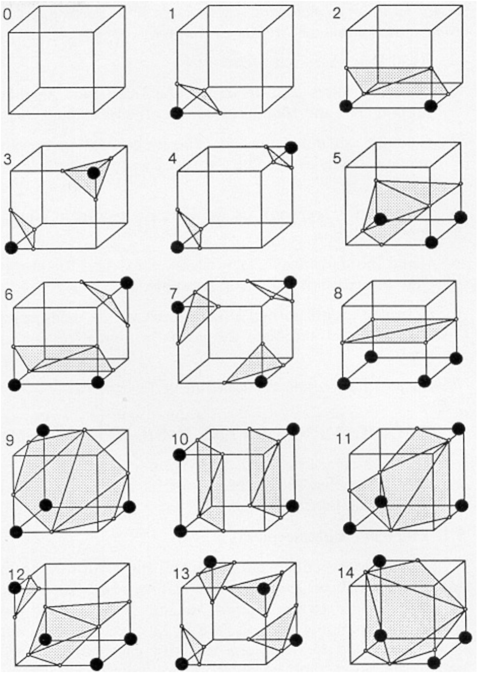

Figure 2.1: Families of triangulated cubes. Marching Cubes method [21].

After this brief introduction on the fundaments of the computation of the surface area and the basics on how the algorithm performs its analysis, we can now present how the total surface area is calculated taking into account the summation of the external side of all the composing triangles of the structure as:

$$SA = \frac{1}{2}\, l_{\mathrm{v}}^2 \sum_i \mid \vec{u}_i \times \vec{v}_i \mid \tag{2.6}$$

for each particular triangle (i) inside a voxel with length l_{v}. $\vec{u}_i$ and $\vec{v}_i$ denote the defining vectors for two of the three sides of the triangles.

On the other hand, the specific surface area (SSA) is defined as the ratio between the previously defined surface area and the total volume of the

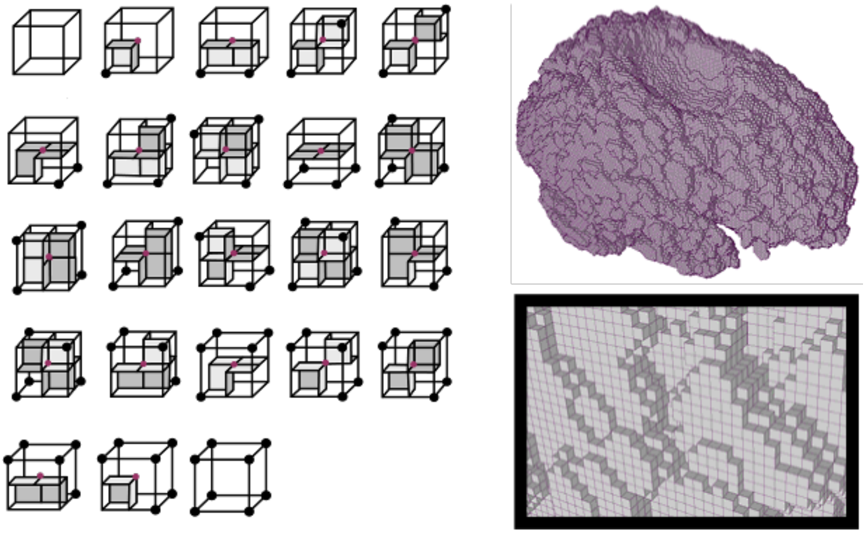

Figure 2.2: Representation of the cuberilles method approach [22].

sample analyzed, presenting therefore the following equation:

$$SSA = \frac{SA}{V} = \frac{\frac{1}{2}\, l_{\mathrm{v}}^2 \, \sum_i \mid \vec{u}_i \times \vec{v}_i \mid}{V} \tag{2.7}$$

where V, the volume of the domain may be obtained as the product of the lengths of each side of the domain, times the cubic voxel length or $V = XYZl_{\mathrm{v}}^3$.

Although been trivially defined, the SSA is an important characteristic in porous ablative materials such as the ones analyzed in this work due to its influence in the reaction rates.

2.1.3 Thermal and electrical conductivities

Thermal conductivity is the measure of the easiness with which a certain medium transmits heat through itself. It is an intensive property of the material and as such, it does not dependent on its shape or dimensions for a homogeneous medium. It defined by Fourier's Law as the amount of heat that is transferred per unit of time and per unit area through a certain material, when it is exposed to a thermal gradient between two opposite sides.

It is usually defined with the Greek letter κ as the ratio between the heat flux and the imposed temperature gradient, and it is formulated as:

$$\mathbf{q}(\mathbf{r}, t) = -\kappa \; \nabla T(\mathbf{r}, t) \Longleftrightarrow q = -\kappa \frac{(T_2 - T_1)}{x} \tag{2.8}$$

where q is the heat flux and x the distance between the measurement of the thermal gradient. In the left-hand equation, a more general approach is presented, with a vector formulation. On the right, the equation is used with scalar values to represent unidimensional simplification. Its units, according to the SI, are $\mathrm{W\,m^{-1}\,K^{-1}}$.

It is fundamental to set a correct distinction among properties of the material make the difference between **intrinsic and effective** characteristics. The former makes reference to the conductivity of each material compounds and phase of the domain, independently on their proportion or orientation. The latter, however, it is the overall value for the whole geometry when accounting all its different material compounds or phase. Effective properties are also called macroscopic or bulk properties, as they will be used in lumped or volume-averaged models.

When computing the effective thermal conductivity of a material, several properties must be previously set up, as it is determined by the material's microstructure and the conductivity of its constituents. If the density of the material is constant, the temperature field can be expressed by the following heat equation:

$$\frac{\partial T(\mathbf{r},t)}{\partial t} = (\alpha \nabla^2 T(\mathbf{r},t)) \tag{2.9}$$

which is known as the Heat Equation.

Here, α is the thermal diffusivity defined as per Equation (2.10). This property describes how quickly a material reacts to a change in temperature. It is a material-specific property for characterizing unsteady heat conduction. Given the density and the heat capacity, one can retrieve the thermal conductivity from this quantity.

$$\alpha = \frac{\kappa}{\rho c_p.} \tag{2.10}$$

From the vectorial solution of the conductivity equation, a 3x3 symmetric tensor is obtained for the effective thermal conductivity of each of the intrinsic thermal conductivities, as the one in Equation (2.11). In this matrix, the main diagonal represented the conductivity of the material in the three main directions (X,Y,Z) and the off-diagonal values, if not-null, will imply cross-coupling and complementary bending of the heat flux, meaning applied flux through a certain axis, being transmitted over the transverse direction, non-unidimensional flux.

$$\kappa_{ij} = \begin{pmatrix} \kappa_{xx} & \kappa_{xy} & \kappa_{xz} \\ \kappa_{yx} & \kappa_{yy} & \kappa_{yz} \\ \kappa_{zx} & \kappa_{zy} & \kappa_{zz} \end{pmatrix} \tag{2.11}$$

κ is the thermal conductivity tensor and κ_{ij} denotes the elements of κ. Usually these materials are considered to be transverse isotropic, meaning that their physical properties are symmetric about an axis, which in this case is considered to be the Z-axis ($\kappa_{xx} \approx \kappa_{yy} \neq \kappa_{zz}$). Because of this reason, the X- and Y-direction are also known as *in-plane directions*, while the normal to them is known as *through-plane direction*. Other nomenclature when referring to conductivity may include, *conductive* and *insulating* directions respectively.

The specific case of the electrical conductivity has not been addressed previously in this section for two main reasons. The first one is that all what has been stated previously for the thermal case applies identically for the electrical case, as the governing equations resemble in the formulation and the Equation (2.9) may be derived to express the electrical conduction as $\nabla \cdot (\sigma \nabla U) = 0$ where σ is the electrical conductivity and U is the voltage potential. Therefore, all the methodologies and solvers are implemented likewise. The other reason is that in the scope of this work, electrical conductivity is not relevant for the study of the decomposition of TPMs.

In order to solve the heat equation (Eq. (2.9)), it was proven by Mugler and Scott [23] that the solution of time-dependent partial differential equations using discrete (i.e. finite difference) versions of those equations may be found using fast Fourier transform (FFT) techniques that treat the solution as the output of a linear filter.

Lastly, it must be clear that even the intrinsic conductivity of the fibers is an intensive property, which is not affected by the quantity of material, in a composite, the effective conductivity is not an additive property, so is not linearly dependent on the proportion of the components, as it is also affected by its geometric distribution. Therefore, it cannot be easily computed for a material like the carbon fiber felts under study.

2.1.4 Tortuosity

The tortuosity factor for a given material is a coefficient that quantifies its resistance to a diffusive flux. This property is used to describe diffusion and fluid flow in porous materials. It is an important property in modeling diffusion-reaction systems, for ablative TPS response [24]. It is usually denoted by the Greek letter τ.

There have been several attempts to quantify this property but in order to better understand this property, a two-dimensional approach (Fig. 2.3a) will be firstly introduced. The simplest mathematical method to estimate tortuosity is the arc-chord ratio, which computes the total length of the curve over the straight-line distance between its ends. Following this definition, an arc-chord ratio equal to one will correspond to an ideal straight path but will tend to infinite for a circular never-ending path. Others suggested that the tortuosity should be measured as the relative change of curvature through the derivative of the logarithm of curve. Because of the subjectivity of the property many approaches have been proposed since the 90s including integration and fractal dimensions to compute it.

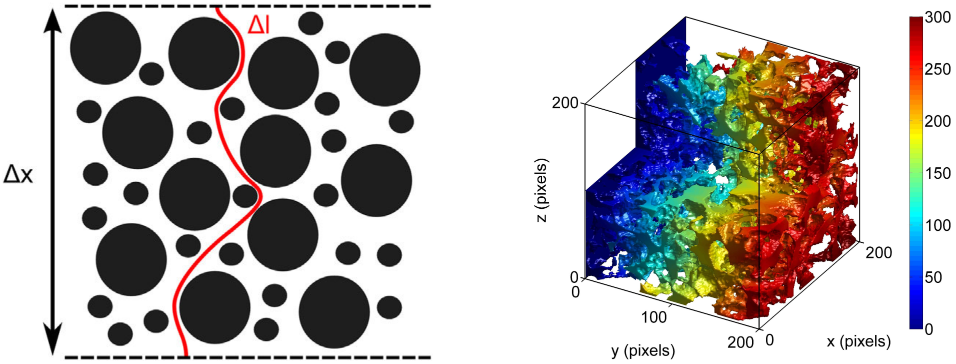

(a) Two-dimensional (b) Three-dimensional

Figure 2.3: Illustrations of tortuous paths through porous networks [25, 26]. On Fig. 2.3b, representation of the shortest distance within the pore space from the left limit to any point, in pixels.

In the three-dimensional domain the problem to correctly compute the tortuosity becomes even greater because of the added degrees of freedom. For solving it, many of the solutions applied on the 2D domains have been proposed and extended. However, in the particular case of this study the tortuosity factor is defined and solved for each direction through:

$$\tau = \epsilon \, \frac{D_{ref}}{D_{eff}} \tag{2.12}$$

being D the diffusion coefficient, where D_{ref} and D_{eff} are the reference and effective diffusion coefficients of the material, respectively. This gives us a formulation in which an increase of the porosity will result in a subsequent increase of the tortuosity. This may seem counter-intuitive, but it is actually bonded by the fraction between the reference and the effective diffusion, which will lead to a unitary value, in case the diffusion is perfect, and will tend to infinite as it distances from ideal. For some special cases it can also take values below the unit, but always showing non-perfect diffusion.

In this case, we can define D_{ref} with the Bosanquet approximation [27]:

$$D_{ref} = \frac{1}{3}\bar{v}\left(\frac{\bar{\lambda}\, l_D}{\bar{\lambda} + l_D}\right) \tag{2.13}$$

as the diffusion coefficient through a capillary of diameter l_{D}, where $\bar{v}$ and $\bar{\lambda}$ are the mean thermal velocity and the mean free path of the gas respectively.

Two cases may rise depending on the Kn. In the continuum, defined by a low Knudsen number (Eq. (2.3)) of the order of 10^{-2}, the Knudsen effects can be neglected as $\mathrm{Kn} = \bar{\lambda}/l_D \ll 1$ so $D_{\mathrm{ref}} = D_{\mathrm{bulk}} = \bar{v}\ \bar{\lambda}/3$. Therefore, the tortuosity may be calculated easily with Equation (2.12). In this case a finite volume or finite difference method can be used to solve the steady state diffusion coefficient D_{eff}. However, when in the transitional or rarefied regimes, this assumption cannot be done and the tortuosity must be solved by using statistical methods.

2.1.5 Representative elementary volume analysis

The Representative Elementary Volume (REV) is defined as the absolute minimum domain volume which will be able to provide a representative value for the characteristics of the whole material when performing an analysis. As one can imagine, when working with porous media, a good REV analysis is crucial to avoid errors due to the intrinsic irregularities of the material. It comes trivially that if the sample size turns out to be too small, the property measured may vary and, as it increases, this variation in the measurements begins to dump until they get stabilized to a certain value as shown in Figure 2.4. For example, let us consider the carbon fiber preform. If the selected domain is of the order of a carbon fiber width, it is possible that the domain is only occupied by either a fiber, or by a gas (or vacuum), thus rapidly varying when changing the domain location in the sample. As the domain becomes larger, it will become more homogeneous until the properties become constant under a given threshold (typically 2%). This will be the value of the REV.

Nevertheless, it can also be observed that for non-homogeneous materials such as rock sediments, once the domain is sufficiently large, we may enter in a third stage of properties variation where macroscopic characteristics may influence the overall results. Therefore, a Maximal Elementary Volume (MEV) is also defined for these cases. However, this will not be addresses in this work study as it does not apply for our type of materials.

2.2 The ZURAM® material and its carbon fiber preform

ZURAM® is a lightweight porous ablator developed by the Institute of Structures and Design of the German Aerospace Center (DLR). It is composed of

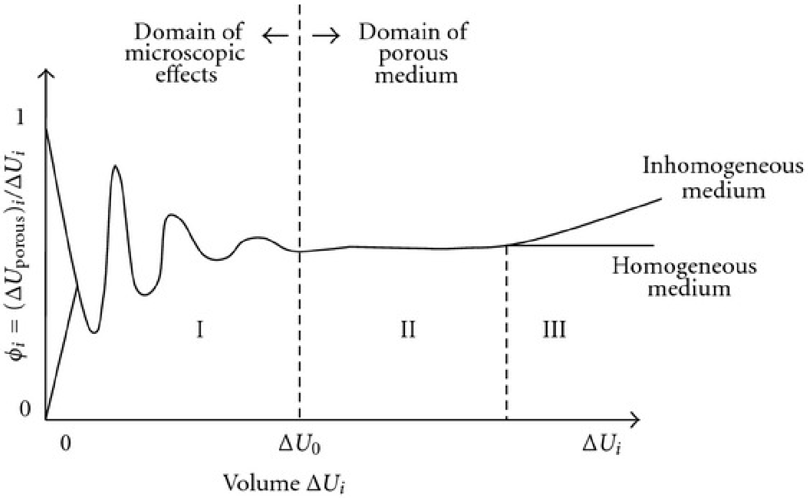

Figure 2.4: Void volume fraction or porosity (ϵ) fluctuations as a function of the sample volume (From Borges [28]).

a rigid carbon fiber preform and a phenolic resin matrix. Since it is designed for high enthalpy atmospheric entry missions, it features low densities of 0.36 to $0.4\,\mathrm{g\,cm^{-3}}$ and high porosities ($\epsilon > 0.8$).

Some research has already been done to characterize its properties, as the developed by Pagan et al. [29] in order to measure its surface recession; Reimer et al. [7], on its mechanical properties; or at the VKI, regarding thermal properties and ablation performance [30, 31, 32]. In this work, the focus will be put on the carbon fibers.

The ZURAM® material has been manufactured in different varieties depending on the ratio of carbon fibers to phenolic resin. Particularly, for this study ZURAM® 18/50 was used. This means a bulk density of the preform carbon fiber material of $180\,\mathrm{kg\,m^{-3}}$ and a proportion of a 50% in mass of phenolic resin.

One of the main advantages of using ZURAM® over other carbon/phenolic ablators for this research is that the material is not subjected to restrictions, hence data and even the material itself can be shared among researchers of different countries. Moreover, as it is composed of a commercially-available preform such as CALCARB® it is feasible to independently study the different phases of the structure —i.e., resin and carbon structure— so particular dedicated analysis can simplify the overall material analysis by isolating/excluding some specific physical processes [33].

CALCARB® is a non-flexible industrial grade carbon-fiber felt, originating from rayon[2], which is usually used as thermal insulation in production furnaces developed by Mersen Scotland Holytown Ltd. It is a high-performance insulator composed of carbon fibers of scarce millimeters in length and a few micrometers in diameter, interconnected by a pyrolyzed phenolic-resin matrix. The precise variation of the preform which meets the requirements of ZURAM® 18/50, is CALCARB® CBCF 18–2000, which presents a bulk density variation of $(0.18 \pm 0.03)\,\mathrm{g\,cm^{-3}}$, a porosity of 89% and less that 20 ppm of metallic residues in its purified version [34].

2.2.1 Properties of carbon fibers

The raw material used to make carbon fiber is called the precursor. This precursor material is then pyrolyzed to obtain the carbon fibers. In industry, about 90% of the carbon fibers produced are made from polyacrylonitrile (PAN). The remaining 10% are made from rayon or petroleum pitch [35]. However, even if PAN-based carbon fiber has the wider and most extended application due to its cost-effectiveness and its high elastic modulus, when rayon fibers are exposed to a carbonization process of heating in the range of 1500 to 2000 K, they exhibit the highest tensile strength and elastic modulus. In addition, the carbon fibers are usually treated at high temperature 2000 K to ensure stability. Moreover, as it was shown by Pradere et al. [36], the thermal conductivity κ also varies depending on the kind of carbon fibers presented. In Figure 2.5, we can observe that TC2 (which refers to rayon fibers such as the ones of CALCARB®) presents the lowest thermal conductivity hence, the best insulating capabilities when compared with the other precursors. These are the main reasons rayon-based carbon fibers are the preferred choice for high-performance insulation purposes in braking systems or heat shields in the aerospace sector.

Taking a closer look to Figure 2.5 the thermal conductivity values measured for this type of fibers between 750 to 1250 K is of the order of 10 to $15\,\mathrm{W\,m^{-1}\,K^{-1}}$, while experiencing a slight increase with temperature.

In order to define a reference value of the intrinsic conductivity of the fibers for the work developed on this material, $\kappa = 12\,\mathrm{W\,m^{-1}\,K^{-1}}$ was chosen to be the average value to best represent the analysis requirements of environmental testing conditions. Furthermore, additional literature was reviewed to check the reliability of these data in other contexts and the values found where between 2.5 to $35\,\mathrm{W\,m^{-1}\,K^{-1}}$ [37]. In addition, it can be seen in Figure 2.5 that when TC2 is previously treated at 2500 K, the fibers present a higher conductivity which may be justified by a graphitization process (further explained in Section 2.3.2).

---

[2] Manufactured fiber, made from natural sources such as wood, obtained as purified cellulose.

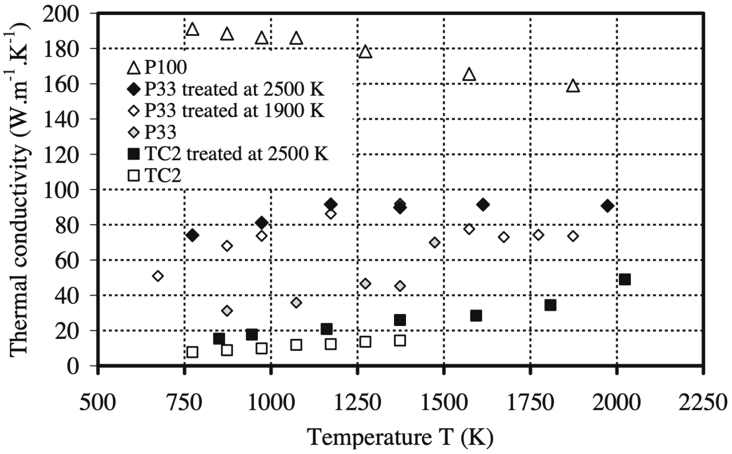

Figure 2.5: Thermal conductivity measurements of rayon-based (TC2), PAN-based (P33) and pitch-based (P100) carbon fibers. [36]

While the intrinsic conductivity defines the conductivity of a single fiber, in porous materials, it is more relevant to obtain the effective conductivity of the bulk material. Nevertheless, this quantity should not be handled heedlessly as will depend on the medium where it is measured. Due to the low porosity of these materials, a large part of the sample, will be either empty (vacuum) or occupied by a gas at a given pressure (typically atmospheric) during conductivity measurements. The values of the bulk thermal conductivity of CALCARB® provided by the manufacturer are reported in Table 2.1 [38]. It can be seen that the conductivity in vacuum is lower than the cases with a gas due to the contribution to the effective conductivity from the gas.

$\kappa_{\text{CALCARB}^{\circledR}}$	400 K	500 K	800 K	1000 K	1200 K	1600 K	2000 K
Argon		0.36		0.54			1.16
Nitrogen	0.45	0.48	0.64	0.72	0.84	1.15	1.47
Vacuum	0.25	0.26	0.35	0.41	0.48	0.69	1.00

Table 2.1: Thermal conductivity [$\mathrm{W\,m^{-1}\,K^{-1}}$] of CALCARB® CBCF 18-02000 at different temperatures.

However, as these data may seem scarce and insufficient to correctly develop and verify the thermal conductivity a quadratic interpolation and extrapolation analysis was performed to obtain the following curves in Figure 2.6

It should be noted that for the three cases a quadratic regression was fit, but while for both the nitrogen and the vacuum environments, the precision is approximate, it can be observed how for the Argon case it adjusts perfectly

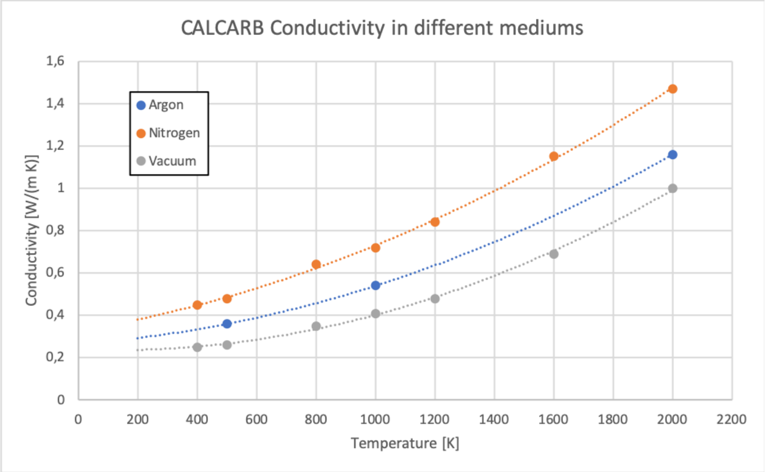

Figure 2.6: Quadratic regressions for the thermal conductivities of CALCARB® CBCF 18–2000 under different environments.

to the given values. This is due to the lack of data, as it should be noted in Table 2.1 that only 3 values are available, and any quadratic equation may be defined by three points. Even though in the case of Argon there were only 3 measurements, for consistency, we kept the same shape for the polynomial.

The choice of the different environments was based on the set of data provided and on the previous knowledge. Therefore, on the one hand, air was selected to be tested as it gives valuable information being the medium for the real applications. On the other hand, the main gases to be used in the experiments for characterization of thermal conductivity are usually Argon, Nitrogen or Helium, but only the former two were selected to be checked as they are the most common ones. Among them, nitrogen is used when temperatures remain under 700 °C, as it behaves as an inert gas. However, nitridation[3] may occur if higher temperatures are reached in which nitrogen dissociation occur [39]. Also vacuum was tested together with the previous presented environments as all of them provide useful characteristics to the set-up, so both inert gases and vacuum avoid reacting with the sample.

Table 2.2: Thermal conductivity [W/(m K)] of different gases as a function of temperature [K].

Gases	200 K	400 K	600 K	800 K	1000 K	1200 K	1400 K	1600 K	1800 K	2000 K
Argon	0,0145	0,0219	0,0298	0,0364	0,0431	0,0483	0,0534	0,0584	0,0634	0,0685
Nitrogen	0,0162	0,0240	0,0326	0,0391	0,0455	0,0508	0,0561	0,0613	0,0664	0,0716
Air	0,0171	0,0253	0,0341	0,0414	0,0490	0,0548	0,0605	0,0662	0,0718	0,0775

---

[3] Exothermal chemical process through which nitrogen reacts with a carbon surface producing CN ($C_s + N \rightleftharpoons CN$).

Even though it can been seen in Table 2.2 that the conductivity of the gases is three orders of magnitude lower than the intrinsic conductivity of the fibers; as it was previously noted the porosity of these materials can be as high as ∼90 %, so in such conditions, the conductivity of the gas becomes relevant.

The values for the thermal conductivity of the different gases were obtained through the VKI's MUlticomponent Thermodynamic And Transport properties for IONized plasmas in `C++` (Mutation^{++}) library [40]. Mutation^{++} has been developed to compute thermodynamic and transport properties of ionized gases including equilibrium compositions and species production rates due to finite-rate elementary reactions. In it, three databases are checked to verify the properties of gases: the NASA 7- and 9-coefficient polynomials and a custom database which describes each atom and molecule as a rigid-rotator and harmonic oscillator.

All the values have also been plotted into a scattered graphic in Figure 2.7 to better understand the trends.

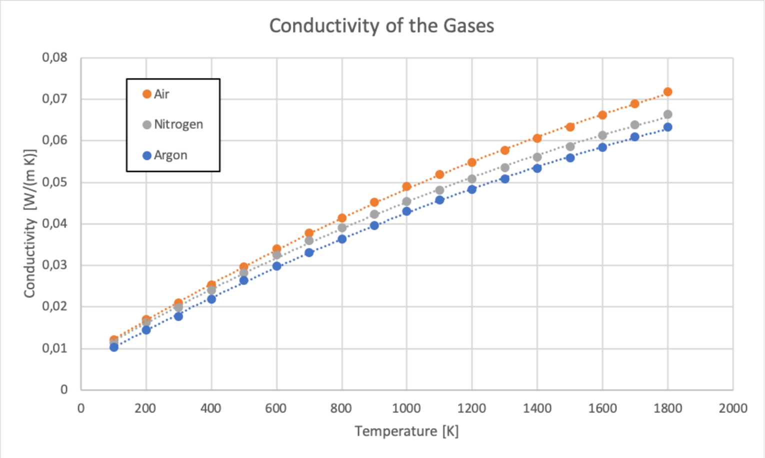

Figure 2.7: Thermal conductivity as a function of temperature for the different gases considered.

2.3 Experimental facilities

Even though this project has entirely been devoted to numerical work, it is important to understand how the empirical values have been obtained and how typical experimental analyses for characterization are performed in order to model the materials. The two facilities that are key to understand this work, are the micro-computed tomography, in order to obtain faithful virtual representations of microgeometries; and the LFA apparatus, which helped with the characterization of the macroscopic properties of the material.

2.3.1 Micro–computed tomography

Micro-computed tomography is a non-destructive experimental technique through which three-dimensional images can be obtained from physical samples of a material, with a micron-level spatial resolution and including its internal structure. Its working principle is based in a setup as shown in Figure 2.8.

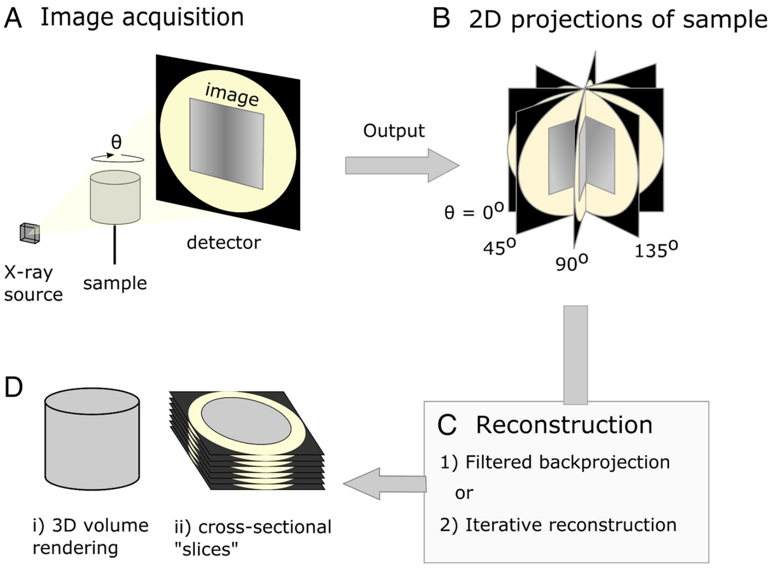

Figure 2.8: Diagrammatic representation of X-ray micro-computed tomography workflow. [41]

Using an X-ray source, pulses are emitted while the sample is rotated at certain increments of θ up to complete a whole turn of 360°. From this pulse, 2D raw images following a gray-scale configuration are projected on the detector and stored. With this, the full geometry can be digitally reconstructed using numerical algorithms [41]. With this procedure, it is possible to represent even the inner part of the fibers to check their microposority or if they are hollow. Finally, once the reconstruction of the volume is done through a filtering iterative process, the 3D volume render is obtained and stored in a TIFF file as stack cross-sectional layers with lossless compression. With this procedure the detail capabilities resemble the shown in Figure 2.9, where even the smallest detail of the carbon fibers can be modeled and analyzed.

This procedure offers great capabilities for research carried out with porous materials such as the ones used in the TPS on the aerospace industry. Its main applications include image processing of microscopically

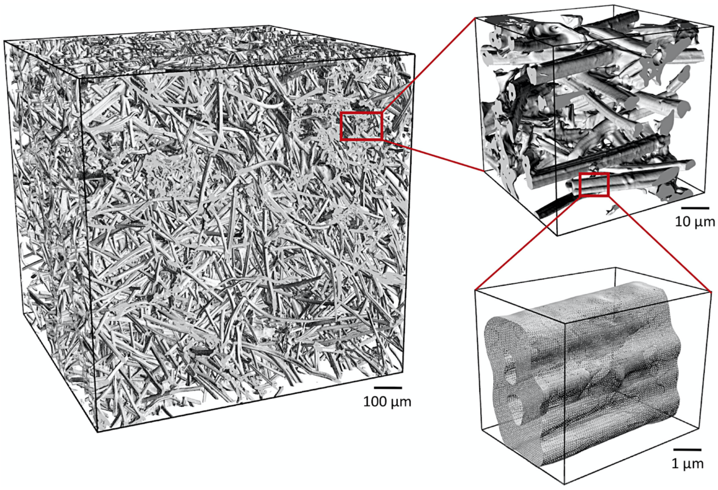

Figure 2.9: Microtomography import and details. [27]

heterogeneous but macroscopically homogeneous structures, the characterization of properties such as porosity of materials, or computational studies of intrinsic properties through specialized software, among others.

2.3.2 Laser flash analysis

Laser Flash Analysis (LFA) is an experimental method used in the industry since the 60s in order to compute thermal diffusivity of materials, even at very high temperatures. A schematic drawing of the main parts and functionalities of the LFA method are shown in Figure 2.10 where it can already be intuited how it works.

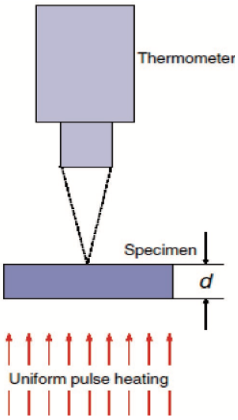

Figure 2.10: Schematic configuration of the LFA method. [42]

In this method, a machined disk sample of few millimeters radius is subjected to a high-intensity short-duration light pulse applied by laser to the front face of the sample. The resultant temperature rise in the opposite side is monitored as a function of time, as seen in Figure 2.11, with an infrared detector, which used with the sample thickness is able to determine thermal diffusivity. If the test follows several assumptions presented by Parker et al. [43] including, adiabatic and homogeneous material, uniformity (both in geometry and in in the heat distribution) or opacity, such that the heat flow may be considered one-dimensional. An analytical solution was proposed by Carlsaw and Jaeger [44] to solve the thermal diffusivity. Applying several simplifications as described in [43], an easy formula Equation (2.14) may be obtained to thermally characterize materials through the LFA method:

$$\alpha = 0.1388\frac{d^2}{t_{1/2}} \tag{2.14}$$

where d represents the thickness of the test specimen at temperature of measurement (in centimeters), and $t_{1/2}$ is the time to reach the 50% of maximum temperature increase, measured at the rear surface of the specimen in seconds. From this measurement, then thermal conductivity may be easily computed if the specific heat and density of the material are known (Eq. (2.10)).

This is an experimental method commonly used for aerospace applications because of the large temperature range, but due to its high complexity and cost, is not always available.

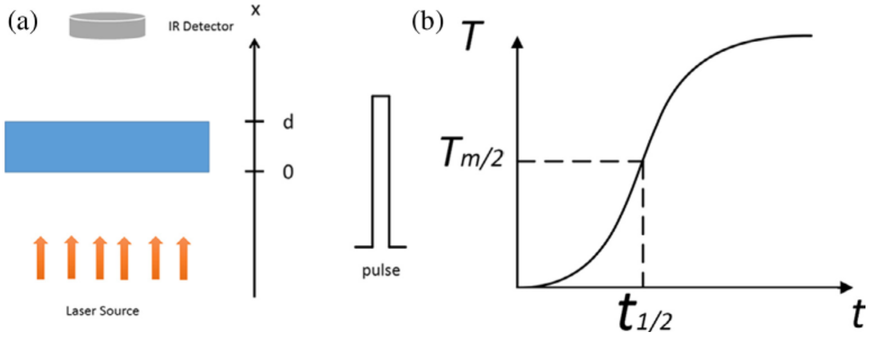

Figure 2.11: Diagram of LFA method. (a) Sketch of data acquisition procedure and (b) Half-time definition from the plot for the temperature rise in the rear side of an LFA experiment. [45]

Chapter 3

PuMA Software

The Porous Microstructure Analysis (PuMA) software is a computational framework in which the characterization of the microstructure of porous materials can be performed with non-invasive methodologies by using digitalized geometries. This software was developed in order to compute effective material properties, such as thermal or electrical conductivities, as a response to the need of correctly simulate the reactions that occur during reentry maneuvers at the surface of the TPS materials when in contact with the atmospheric gases [21]. The software was written in `C++` for Linux operating systems and it is optimized for multi-processor workstations. It is available as open source NASA software under a US & Foreign release [1] as it is being continuously developed by the NASA Ames Research Center.

PuMA is a genuinely powerful tool which allows not only to generate simulated microstructures of the samples to be studied but also to import them as a TIFF image obtained through a microtomographic scan of the real material, as explained in Section 2.3.1. In that way, the computational study can be more accurate by using the actual geometry of the material, with its defects and particularities.

Once the sample is modeled and its main characteristics (such as its porosity or specific surface area) are computed, the geometry might be displayed through a 3D-visualization built-in toolkit. However, the main attractive of the PuMA software are the determination of the effective properties of the sample and implementation of the oxidation simulations of fibrous materials.

In this work, PuMA V2.2 (Fig. 3.1) has been used as the main tool to perform the thermal characterization of porous materials through a parametric analysis of literature-based artificially-generated geometries and to represent an LFA test campaign.

---

[1] https://software.nasa.gov/software/ARC-17920-1

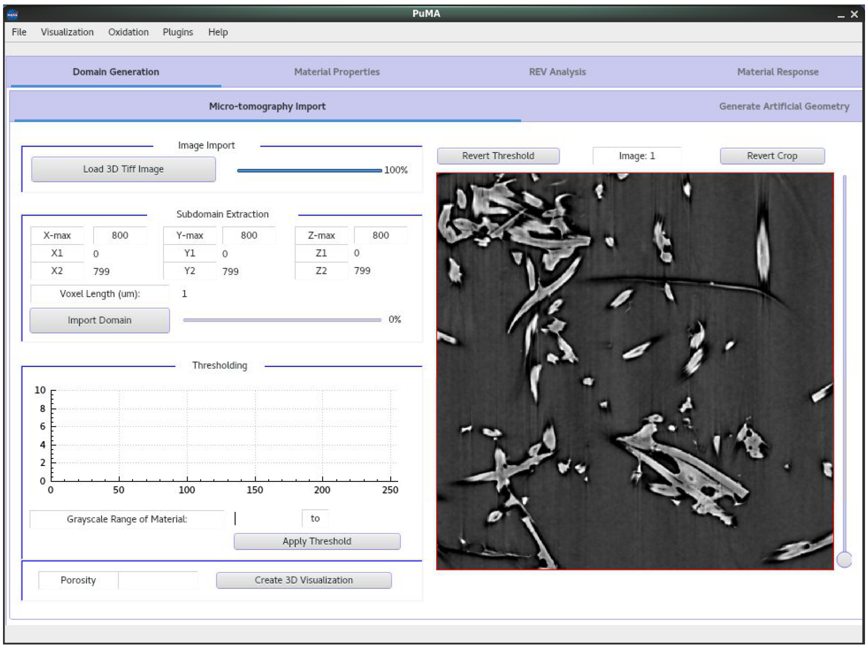

X-max 800
X1 0
X2 799
Y-max 800
Y1 0
Y2 799
Z-max 800
Z1 0
Z2 799
Voxel Length (um): 1
Image: 1

Figure 3.1: Graphical User Interface of PuMA V2.2

3.1 Domain Generation

A computational domain in PuMA may be constructed either artificially by introducing the corresponding data for the appropriate set up, or imported as a 3D TIFF image. Both options will be presented below.

3.1.1 Microtomography import

PuMA is capable of generating 3D geometries from real materials by importing stacks of TIFF images obtained through X-ray micro-computed tomography.

Once a 8 or 16-bit TIFF image has been loaded into PuMA, the software allows the user to define the size of the sample that will be analyzed and the length of the minimum representative volumetric value on a 3D space, also known as voxel[2] that will depend on the resolution of the sample provided. Moreover, once the microtomography has been imported, a gray-scale histogram helps the user to identify the different phases on the material depending on their density. This in useful when defining the cutoff range for each of the different materials of the sample. Once all this is accomplished, the domain may be processed using the Marching Cubes Algorithm explained

---

[2] As pixel stands for picture element, voxel is for volume element.

in Section 2.1.2 and visualized. This way, its porosity may be obtained.

3.1.2 Artificially generated model

Another possibility offered by PuMA is to artificially generate geometries that simulate the material to study. Other options include the generation of different theoretical geometries as a cylinder, a box, a sphere or a packed sphere bed. The user interface and the options available may be observed in Figure 3.2.

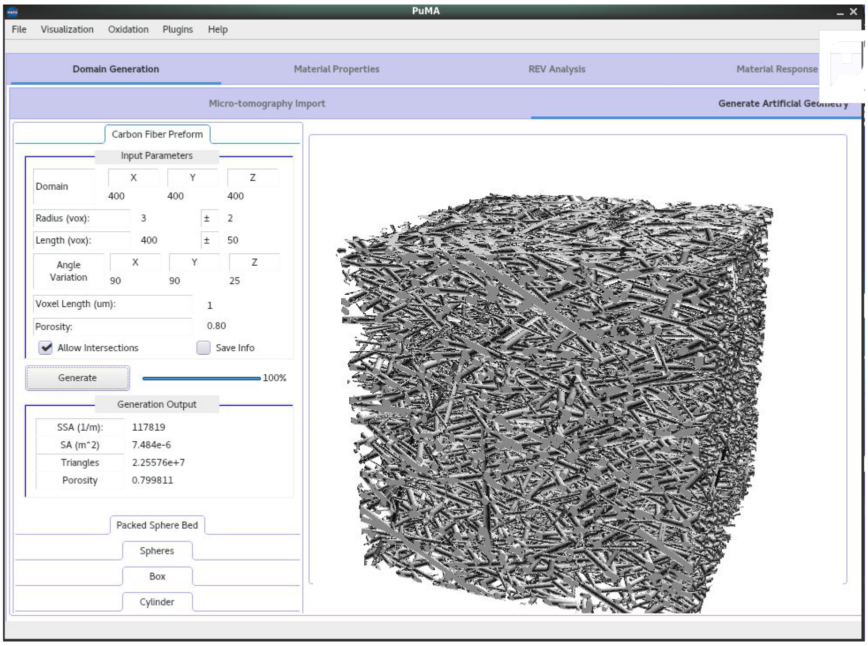

	X	Y	Z
Domain	400	400	400
Angle Variation	90	90	25

Radius (vox): 3 ± 2
Length (vox): 400 ± 50
Voxel Length (um): 1
Porosity: 0.80
☑ Allow Intersections ☐ Save Info

SSA (1/m): 117819
SA (m^2) 7.484e-6
Triangles 2.25576e+7
Porosity 0.799811

Figure 3.2: PuMA's Carbon Fiber preform artificial-geometry generator GUI

In this work, the carbon fiber preform generator was mainly used. In this mode, the software generates a typical carbon fiber preform by randomly placing perfect cylinders which simulate the fibers. As inputs, the user defines the domain size, the voxel length in microns, the radius and the length of the cylinders in voxels plus their variation, the porosity of the material and the maximum angular orientation of the fibers in each direction.

When creating an artificial domain through the input parameters, automatically a generation output prompts out in the same screen (Fig. 3.2) in the lower-left corner where accurate values for the model's specific surface area (SSA), surface area (SA) and porosity are obtained. In this case, porosity must be recalculated as, when generating the domain the number of cylinders is a function of the porosity, but they will be placed randomly until an approximate value for the porosity is reached. Nevertheless, if the `Allow`

`Intersection` box is not marked, the software will need to iterate over the domain in order to fulfill the porosity and fiber dimensions constraints while allocating the fibers, thus increasing the computational cost.

Artificially generated models can also be saved and stored as a TIFF stack for their import in further analyses. If the `Save Resulting Map` option is checked, a 3D tiff containing the steady state temperature at every point in the domain will be saved within the run folder under /Conductivity Maps. The image will be saved with T (indicating temperature) along with the simulation direction. These values are intended to be used for visualization purposes and have therefore been normalized to between 0 and 256 to be saved within a 16-bit TIFF image.

It shall be noted that the geometries are always generated randomly from scratch by a pseudorandom number generation (PRNG) using a seed number between 0 and 0xFFFFFFFF. However, the user cannot change this number, thus each time the software generates a geometry, even with the same set of parameters, it will be slightly different.

3.1.3 Darcy's law application

Once it has been shown how the domain can be correctly generated or imported with high detail and precision, is understandable why the approach shown at Chapter 2 to solve porous volumes by averaging properties is not required.

The methodologies used in PuMA are based on an algorithm developed by Lachaud and Vignoles [46] where the gas-surface interactions during ablation are simulated by a Brownian motion with presents special Random Walk rules close to the fibers to efficiently simulate mass transfer in low Péclet numbers (Pe). Also a sticking probability law has been obtained for modeling heterogeneous reactions. And the degradation of the carbon fibers is being tracked by a simplified marching cubes discretization.

Besides, when comparing PuMA to other software developed for the same purpose with similar characteristics it is easily noticeable that the latter are focused on the analysis of reduced data sets with limited temperature ranges, not able to properly be representative of the real space applications.

3.1.4 Domain size

The correct selection of the size of the domain is critical as unlimited computational memory is not always available. X-ray microtomography data-sets with high resolution may be relatively large, with an order of magnitude of several billion voxels (with typical file sizes in the order of 15 GB). As both the electrical and thermal conductivity solvers used in PuMA require the use of the FFT method to compute the Fourier transform of the matrices, the simulation speed will be highly dependent on the length of the matrix. Usually, in order to obtain the fastest results the size of the domain should be a power of 2. This reason comes as what it is intended to achieve is to minimize the largest prime factor of the domain size in each direction. This means that when decomposing the value into its prime factors, we should try to reduce as much as possible the greatest of these values. That is why powers of 2 are the ideal, but values as 600 or 864 may also present fairly good velocities. It is also important to take into account that when importing a domain, as PuMA has been written in `C++`, the domain range should be between zero and $(2^n - 1)$. Otherwise, the result would be the opposite of the expected as domains with $(2^n \pm 1)$ voxels in length will usually unveil the largest prime factors.

3.2 Material's properties

From this point on, the model will be presented as if it was imported from a TIFF stack but taking into account that there is no difference in the following steps between that case and the artificially generated one, as the latter may also be saved and stored for a subsequent analysis.

3.2.1 Porosity

PuMA calculates the porosity of the imported material based on a three-dimensional matrix of gray-scale values. Taking this into account, the volume fraction of a phase i of the material is computed using Equation (2.4) but taking into account $\phi = \frac{N_i}{N_{\text{tot}}}$ as the ratio between its number of voxels and the total. Therefore, it is straightforward that $\phi_{\text{void}} = \epsilon$.

3.2.2 Surface area and specific surface area

Both the surface area (SA) and the specific surface area (SSA) of the sample are calculated in PuMA with by the Marching Cubes Algorithm presented in Section 2.1.2.

3.2.3 Thermal and electrical conductivities

Solvers and boundary conditions

In the PuMA software, three different ways have been implemented to solve the steady-state heat (Eq. (2.9)): a simple finite difference (SFD) method, an Explicit-Jump finite difference (EJFD) method developed by Wiegmann et al. [14, 47], and a random walk method. This last method is more general that can be used at any Knudsen number. In it, diffusion is simulated by giving random velocity vectors to individual particles and imposing a free path based on an exponential distribution. However, when working in normal conditions such as atmospheric pressure and temperature, the Knudsen number is very low, so the continuum assumption is widely accepted. Since when taking this kind of assumptions, the finite difference solver is always valid and is much faster, low Knudsen number simulations are rarely run using the random walk model, as they will show the same results with a minor variance. Therefore, the random walk method is not necessary to be used for the purpose of this experimentation. Nevertheless, it is implemented in the PuMA software as it was designed to compute material properties for heat shields on atmospheric reentries were the transitional or rarefied regimes apply.

When analyzing the other implemented methods, the two finite difference methods compute the effective conductivity of a composite material by imposing a 1 K temperature gradient and solving it for the steady-state temperature field at every point. Then, from it, the steady-state heat flux can be determined and used to solve for the effective conductivity of the material.

One of the main differences between the simple finite difference method and the Explicit-Jump method resides in the implementation of the boundary conditions. While the SFD uses Dirichlet boundary conditions in the simulation direction, and periodic or reflective boundary conditions in the side directions; the EJFD one uses periodic boundary conditions in both the simulation and side directions. That may be one of the main reasons why when comparing the studies done with both methodologies, the results may slightly differ.

Dirichlet boundary condition specifies the values that a solution needs to take along the boundary of the domain. It is widely used in situations where a surface is held at a fixed temperature. On the other hand, a periodic or cyclic boundary condition is used if a component has a repeated pattern in flow distribution more than twice. The last one, symmetric boundary condition applies a mirror image between both sides of the domain.

Another important difference between both methods regards the resources consumption and the time employment. The former uses a regular numerical approach to solve the heat equation, by approximating all the derivatives by finite differences. On the other hand, the Explicit-Jump method uses a solver specifically developed for the effective heat conductivity of composite materials so it is a highly efficient and automated method to compute large 3D images on state-of-the-art desktop computers without the need for any further processing [14]. Therefore this method is considerably faster than the SFD method. Moreover, it is known, as it is proven by Crank [48], that in order to solve the heat equation the explicit method is numerically stable and convergent provided that the time-step is always smaller or equal to half the space-step squared $\delta T^2 \leq \delta x^2/2$.

Other factors that may induce differences into our study may come from other physical effects, such as convective or radiative heat transfer, imprecisions in the modeling or inaccuracies in the microtomographies (real or simulated), to name a few possible sources.

3.2.4 Tortuosity

In PuMA, two types of solvers have been implemented to compute the tortuosity factor, which use will depend on several factors and will be presented hereby.

The numerical methods to be used, depend basically on the Knudsen number. This means, if the medium can be considered in the continuum regime, it can be solved using typical numerical methods such as finite volume and finite difference. In PuMA, both an explicit jump and a finite volume solver have been implemented. If the medium is considered to lay into the characteristics of the rarefied regime, it must be solved using particle methods to account for Knudsen effects. Again in the particular case of PuMA, a random walk solver was implemented.

Solvers and Boundary Conditions

In a similar way as it was implemented for the conductivities, also for the tortuosity a finite difference method can be used to solve the equation numerically as presented in Section 2.1.3, when the continuum assumption applies, and a random walk method is implemented that can be used for any Knudsen number, but is specifically applied for the rarefied regimes. In it, individual particles are given a random velocity vector and free path based on an exponential distribution and symmetric boundary conditions are used for particles that exit the domain.

A certain particularity of PuMA is that the tortuosity factor is defined as a geometric property instead of as a function of Kn. In order to verify that, the characteristic length l_D must be established, so a prior simulation with high Knudsen values must be run. This is required in order to solve the Bosanquet equation (Eq. (2.13)) for l_D which assumes that a single value for the characteristic length can be used at all Knudsen numbers [49].

To conclude, it is important to note that, even it might seem trivial at first sight, it has been demonstrated by Espinoza-Andaluz et al. [50] that the tortuosity increases when the porosity decreases, as it will be measured and discussed in this document later on.

3.3 Representative Elementary Volume analysis

Another fundamental characteristic of the PuMA software is the possibility of measuring the representative elementary volume (REV) of a certain geometry. The importance of this parameter resides in the identification of the minimum microstructural domain which allows to represent the material in order to the analysis to be repeatable while using the minimum amount of computational resources as possible.

In PuMA, it is a really critical value because as it has been previously presented in section 3.1.3, it does not use a volume-averaged approach as other software, but directly the microstructure itself.

It is important to note that the REV is dependent on the material property of interest [27]. Due to this reason, a specific analysis may be run for each of the properties to be tested and the effective REV will be the greatest of all of them. In PuMA, when performing the analysis, the user is able to specify both the minimum normal standard deviation when convergence is reached and the several sub-domain sizes in which it will be analyzed. However, the maximum size to test must be as big as half the total domain size, so if the standard deviation is not reached in that range, it will be extrapolated. A typical REV analysis will resemble to what is shown at Figure 3.3. This limitation comes from the fact that PuMA bases its REV analysis on the computation of the selected parameters from sub-domains of the imported total domain. Therefore, the smaller the side length to verify, the longer it will take to obtain the results, as the bigger the number of independently available subdomains will be possible to combine.

Same efficiency remarks should be done regarding the REV analysis as previously presented, so it is important that the choice of the side length for the subdomains to analyze, minimizes the maximum prime factor for faster calculations.

One last note should mention that, normalized standard deviation should be an asymptotically consistent estimator, as it should tend to zero to the extent that the domain size approaches infinity. However, the numerical error of the method used in the solver must be also accounted into the computation of the standard deviation.

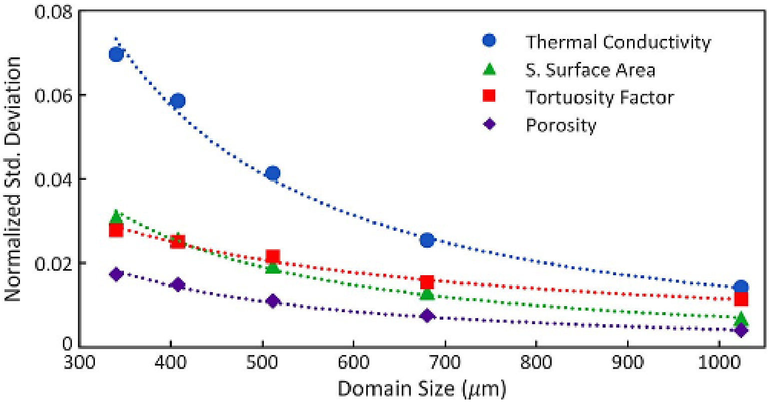

Figure 3.3: REV analysis on a 2000 voxel^3 sample of artificially generated isotropic random fibers [27].

3.4 Simulation inputs and outputs

Inputs

PuMA permits the input of several other structural and computational parameters which allow to perform calculations in a more flexible way and tries to adapt to the necessities of many different cases.

When working on the software, it allows to select which are the properties for each phase —up to six— of the material. In that way, the intrinsic thermal or electrical conductivity may be included as inputs manually or even as a preloaded text file, possibility which allows to verify the behavior of the effective properties as those change.

As it can be seen in Figure 3.4, also the accuracy of the solver and the number of threads to be used are an input. A usual value for the accuracy is of a 0.1%, while the number of threads must be set to the number of physical cores available in order to optimize the calculations. Also the choice of computing properties just in the desired directions for the case of isotropic or transverse-isotropic materials is available.

Finally, an option to store the resulting property's map allows to save the steady state variable —temperature flow, either voltage potential, current flow, concentration, etc...— through the material at every point. All these data will be stored as 16-bit tiff files containing the steady state float values at every point in the domain with the scope of being modeled in a 3D-viewer as Paraview [51].

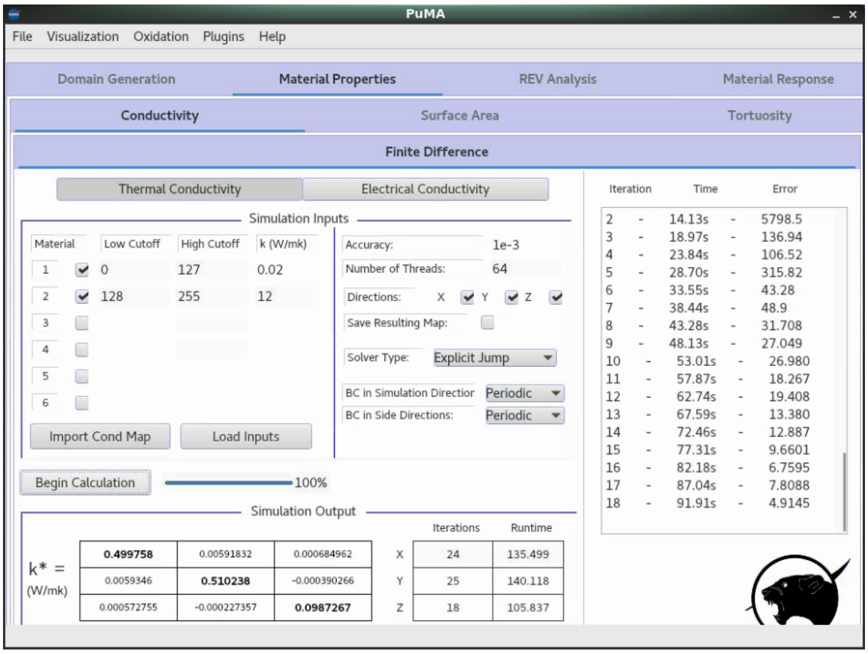

Material		Low Cutoff	High Cutoff	k (W/mk)
1	☑	0	127	0.02
2	☑	128	255	12
3	☐			
4	☐			
5	☐			
6	☐			

Accuracy: 1e-3
Number of Threads: 64
Directions: X ☑ Y ☑ Z ☑
Save Resulting Map: ☐
Solver Type: Explicit Jump
BC in Simulation Directior Periodic
BC in Side Directions: Periodic

k* = (W/mk)

					Iterations	Runtime
	0.499758	0.00591832	0.000684962	X	24	135.499
k* = (W/mk)	0.0059346	**0.510238**	-0.000390266	Y	25	140.118
	0.000572755	-0.000227357	**0.0987267**	Z	18	105.837

```
Iteration      Time        Error
2    -    14.13s    -    5798.5
3    -    18.97s    -    136.94
4    -    23.84s    -    106.52
5    -    28.70s    -    315.82
6    -    33.55s    -    43.28
7    -    38.44s    -    48.9
8    -    43.28s    -    31.708
9    -    48.13s    -    27.049
10    -    53.01s    -    26.980
11    -    57.87s    -    18.267
12    -    62.74s    -    19.408
13    -    67.59s    -    13.380
14    -    72.46s    -    12.887
15    -    77.31s    -    9.6601
16    -    82.18s    -    6.7595
17    -    87.04s    -    7.8088
18    -    91.91s    -    4.9145
```

Figure 3.4: Example of what the user's interface may look like when working on the thermal conductivity analysis.

Outputs

Once the simulation has been completed, the thermal and electrical conductivities and the tortuosity will be displayed side by side to the run-time and number of iterations at the bottom of the user's interface, as may be seen in Figure 3.4. Values of the effective conductivity tensor are provided in matrix notation. The calculated values, as well as the simulation inputs, are always stored into the log file.

3.5 Limitations

PuMA has been shown to be a very complete and versatile software for the characterization of porous materials and its microstructures. It allows the user to compute a wide variety of micro and macroscopic properties of the material of study as the porosity, SSA, thermal and electrical effective conductivities, tortuosity factor, and REV, from a sole microtomographic sample. However, the main particularity that the software lacks is the ability to measure —or to take into account— the radiative effects.

Even the heat transfer by radiation at low temperatures is not significant and is usually neglected, that is not the case when temperatures arise.

In fact, radiation itself is a particular effect when compared with conduction/diffusion or convection, due to the fact that it can transmit heat within a vacuum environment without a direct physical lint between two points, and because this transfer is not just proportional to the gradient of temperatures between both points but also dependent on the absolute temperature of themselves as the radiative transfer between two objects, is defined by:

$$\phi_{\mathrm{q}} = \varepsilon \ \sigma \ F_{12} \ (T_2^4 - T_1^4) \tag{3.1}$$

where ε represents the emissivity of the object, σ is the Stefan Boltzmann constant, whose value is $5.67 \times 10^{-8}\,\mathrm{W\,m^{-2}\,K^{-4}}$, and F_{12} is the view factor, which is the proportion of the radiation leaving surface 1 and reaching surface 2. Typically, to take into account the radiation effects a ray-tracing like algorithm would be needed however, this has not been tackled in the current work.

Another main limitation of the software, and of the solver to be more specific, is the selection of the boundary conditions, as the software does not give the opportunity to select among them freely, but they come imposed by the type of solver used.

Extra disparities between the software and the real model may include the thermal expansion of the material as a function of the temperature, that may influence values as the porosity and the conductivity; and the metallic impurities that the furnished material may present which, even though being very scarce, due to their high thermal conductivity may slightly influence the results.

Chapter 4

Preliminary Study

In this first part of the work, the main scope of the study will be to determine the effect of microstructural properties of porous ablative materials on their macroscopic model characteristics. In this way, it will be aspired to define how the modification of some properties such as the porosity, the fibers' orientation, and both the medium's and the fibers' conductivities affect to the variation effective thermal conductivity and tortuosity and up to which extent. To round out these analyses, several sets of tests will show the REV analysis performed and the descriptive statistical analysis to check its validity. Moreover, a brief study will be presented on how the properties vary when using the different available solvers with their respective boundary conditions; and lastly, a comparison with the real material data provided by Mersen [34, 38] will be done in order to show the validity of the results, and possible improvements. The simulations of this work were performed in an 8-CPUs 32GB RAM Workstation at the VKI, and at the Hydra cluster of the VUB/ULB with 20-CPUs and 80GB of RAM.

4.1 Synthetic material model

Based on the little reference data available of CALCARB® CBCF 18–2000 [34, 38] a synthetic material model has been designed to mimic it. This model was generated using the Carbon Fiber Preform tab showed at Figure 3.2 to generate the geometry presented at Figure 4.1. This sample displayed the following characteristics:

- Domain: 600 x 600 x 600 voxels
- Radius: 7 ± 2 voxels
- Length: 550 ± 200 voxels
- Angle Variation: 90 x 90 x 20 °
- Porosity: 0.89
- Voxel Size: 1 µm

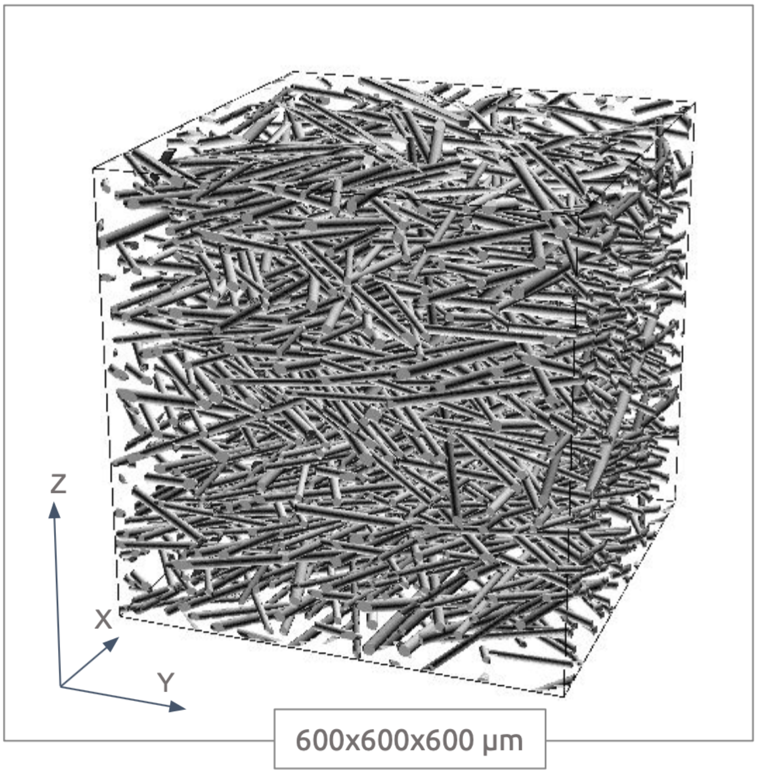

Figure 4.1: Base artificially-created model.

An average length of $l_\mathrm{f} \approx 550\,\mu\mathrm{m}$ and diameter $d_\mathrm{f} \approx 6.5\,\mu\mathrm{m}$ of a single fiber of CALCARB® CBCF 18–2000 were measured by means of Scanning Electron Microscopy (SEM) by Helber [39]. Since only integer values can be inserted, the radius was rounded up. As fibers are not perfect and sometimes, they might adhere in bundles of conjoint fibers or break, a ±30% variability range was decided. Typical values of porosity for carbon fiber preforms range between 0.85 and 0.92 [52, 39], so an average value of 0.89 was selected. Lastly, the angle variation for orientation of the fibers of CALCARB® CBCF 18–2000 has not been found in literature. Therefore, it was chosen to be plus-minus 15 to 20° in the Z-plane angle, mimicking the alignment of fibers seen in Fiberform, the carbon preform of the phenolic/ablator PICA [21]. Also taking into account that it should behave as a transverse isotropic material, a random distribution of fibers was input for X and Y-directions (90°).

The reasons to choose the domain's size —although they were already introduced in Section 3.1.4 and will be further studied in Section 4.2.2— were selected trying to generate an optimal sample to comply with the Representative Elementary Volume, while minimizing the computational resource consumption and being limited by the available RAM.

4.2 Verification of the model

In this section, the different studies preformed in order to numerically characterize the properties of the artificially-generated geometry will be presented and discussed. In it is expected to obtain some results to more efficiently reproduce the following analyses and be able to correctly interpret their results.

All the developed analysis were performed within the three main direction (X, Y, Z) —even if the structure was designed as a transverse isotropic material— in order to check for possible diversions in ideally-identical patterns. Also, for all the studies a common accuracy of 10^{-3} was considered to be enough.

4.2.1 Explicit vs. Simple Finite Difference method

At first, a comparative analysis between the two methods available to solve the heat equation Eq. (2.9) in order to check if there were significant discrepancies in the results. In order to do so, different domain sizes, different porosities of the model, different Z-angle orientations and different intrinsic conductivities for both the medium and the fibers were analyzed.

Table 4.1: Comparison between explicit and SFD solvers for thermal conductivity. All samples present a fiber's conductivity of $12\,\mathrm{W\,m^{-1}\,K^{-1}}$, a conductivity of the medium of $0.017\,72\,\mathrm{W\,m^{-1}\,K^{-1}}$ and 20° fibers' orientation in Z-direction.

	Porosity	Size	Time [s]	Δ %	κ_X	Δ %	κ_Y	Δ %	κ_Z	Δ %
Explicit	0.89	400	61		0.2945		0.2951		0.0687	
SFD	0.89	400	4055	6547%	0.4014	36%	0.4177	42%	0.0676	-2%
Explicit	0.89	600	214		0.4929		0.5159		0.1002	
SFD	0.89	600	16595	7655%	0.4317	-12%	0.4539	-12%	0.0845	-16%
Explicit	0.92	400	64		0.1562		0.1447		0.0417	
SFD	0.92	400	4840	7463%	0.2361	51%	0.2230	54%	0.0400	-4%
Explicit	0.92	600	229		0.3262		0.3314		0.0760	
SFD	0.92	600	20915	9033%	0.2912	-11%	0.2972	-10%	0.0626	-18%

When closely studying the values from the data collected on Table 4.1, it can be seen how the variation between both solvers is reduced as the domain size increases. It can be checked that it is limited (∼10 %) for a domain with the model properties, but it will presumably be even more reduced for a bigger domain, as it will be attributed to the results of the REV analysis presented on Section 4.2.2.

Table 4.2: Comparison between explicit and SFD solvers for thermal conductivity. All samples present a fiber's conductivity of 12 W m^{-1} K^{-1}, a conductivity of the medium of 10 W m^{-1} K^{-1} and 20° fibers' orientation in Z-direction.

	Porosity	Size	Time [s]	Δ %	κ_X	Δ %	κ_Y	Δ %	κ_Z	Δ %
Explicit	0.85	400	17		10.2303		10.2303		10.2214	
SFD	0.85	400	279	1541%	10.2302	0%	10.2300	0%	10.2213	0%
Explicit	0.85	600	60		10.2302		10.2302		10.2210	
SFD	0.85	600	1106	1743%	10.2302	0%	10.2302	0%	10.2210	0%

Table 4.3: Comparison between explicit and SFD solvers for tortuosity. Fiber's conductivity of 12 W m^{-1} K^{-1}, medium's conductivity of 0.017 72 W m^{-1} K^{-1} and 20° fibers' orientation in Z-direction.

	Porosity	Size	Time [s]	Δ %	τ_X	Δ %	τ_Y	Δ %	τ_Z	Δ %
Explicit	0.89	400	28		1.0760		1.0738		1.1231	
SFD	0.89	400	249	789%	1.0752	0%	1.0721	0%	1.1256	0%
Explicit	0.89	600	108		1.0801		1.0774		1.1313	
SFD	0.89	600	901	734%	1.0804	0%	1.0772	0%	1.1318	0%
Explicit	0.92	400	22		1.0521		1.0508		1.0864	
SFD	0.92	400	210	855%	1.0520	0%	1.0508	0%	1.0861	0%
Explicit	0.92	600	99		1.0559		1.0552		1.0905	
SFD	0.92	600	784	692%	1.0558	0%	1.0554	0%	1.0904	0%

For the tortuosity case, it could be easily foreseen that the selection of the solver would not be greatly affecting the calculations and the results obtained from them.

Nevertheless, as it was expected, the most determining factor why it was finally decided to perform the whole set of analysis with the Explicit solver was the time consumption. Tables 4.1 to 4.3 depict how for both the conductivity and the tortuosity calculations, there is a huge influence of the type of solver selected on the time required to obtain the results. It can be observed a reduction in the time required of the order of 50 to 100 times for the range of studies intended to be performed[1].

It must be noted that as the porosity and the angular range increased, also the time required slightly increased. Also, obviously, as the domain size increased, the time consumption increased with it. However, it in Section 4.2.2 the reasons for the election of the domain size were already presented.

---

[1] For the conductivity analysis. For the tortuosity it ranges between 5–10 times.

Therefore, for the whole following part of this work, the Explicit solver will be assumed to be used unless otherwise is specified.

Also it was noted, as expected, from Table 4.3 that when the conductivity of both the medium and the material are closer together, the faster the stability is reached and the lesser are the divergences between the two methods.

4.2.2 Representative Elementary Volume

As it was previously introduced in Section 2.1.5, the PuMA software includes the possibility of analyzing the validity of a certain domain size for imported sample. With the Representative Elementary Volume (REV) analysis of a certain geometry we can identify if the selected domain length is appropriate to correctly represent the overall material's properties of interest.

Taking advantage of this capability, the minimal representative size was tried to be achieved in order to reduce the computational resources. In order to do that, a brief initial analysis was performed over the desired characteristics of the material by just modifying the porosity and the fiber's orientation between their maximum and minimum chosen value for the study, and in each of the cases, varying the thermal conductivity of the medium. Then, the REV analysis was performed for the variables of interest: Porosity, Specific Surface Area, Thermal Conductivity and Tortuosity.

To obtain the most realistic values, the biggest domain size was tried to be generated, but due to limited computational resources $600^3\ \mu m^3$ was the biggest domain size possible by optimizing the prime numbers.

We must note that the different analyses shared common characteristics. The conductivity of the fibers was always set to $12\,\mathrm{W\,m^{-1}\,K^{-1}}$ and the accuracy for the solver of the heat equation was inputted to 10^{-3}. Also the domain sizes selected for the analyses were all powers of two (64, 128, 256) to optimize the time required, and the criterion for REV (Norm. Std. Dev.) was decided to be of a 2%.

The estimated REV value differs for each of the four properties (Fig. 4.2). It can be seen that both the porosity and the tortuosity converge rapidly and reach lower-than-2% standard deviations for domain sizes of under 256 µm for all the analyzed cases. Even if the SSA's REV value exceeds the available domain, the main problem was encountered when checking the thermal conductivity of the material, because its REV values fall far over 1000 µm. Through these analyses an approximate order of magnitude of the error which will be obtained can be extracted. In these cases, it was obtained an uncertainty of the order of a 10–20% depending on the variables for the greatest domain analyzed, 265 voxels.

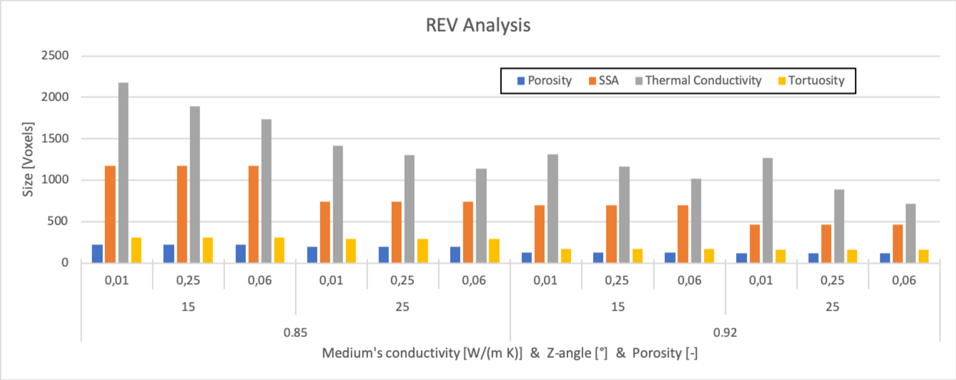

Figure 4.2: Data extracted from the initial REV analyses (St. Dev.= 0.02) performed over the extreme cases to be studied.

It shall also be noted from these first analyses that an increase of the porosity, of the distribution of the fibers in the Z-direction, or of the medium's conductivity has a positive effect in the reduction of the REV, and therefore, a reduction of the uncertainty of the computations on our model. Also we shall note that an increase of a 10% on fibers distribution is grossly equivalent as the increase of a 5% the porosity, for the REV size reduction.

4.2.3 Statistical analysis

A descriptive statistical analysis was designed over the main model with the selected parameters in order to check the validity of the outcomes. This analysis was required because of the inability to generate a sufficiently big geometry for accomplish the REV for our imposed conditions and the impossibility to select the seed to generate the pseudorandom structures. Therefore, the main objective of this part was to verify that the results reside in a certain threshold for the standard deviation, and the conclusions of the work can be reasonably trustful with the limited computational power.

Nine different geometries (NSD1–NSD9) were created with the same identical characteristics previously exposed at Section 4.1, and always using the same thermal conductivity values for both the fibers and the medium: 12 and $0.017\,72\,\mathrm{W\,m^{-1}\,K^{-1}}$ respectively. The porosity was always double-checked to verify that that its variation was smaller than a 0.01% because of the iterative process to generate the geometry for each single case. Then, a regular statistical study was performed to obtain for each of the variables the variance, the standard deviation, the average value of the sample and its variation. All these values can be found in Table 4.5.

After taking a closer look to the test performed, it can be verified that the variation remains under the 2% value that was set as a threshold, except for the thermal conductivity in all the three direction, but especially for the Z-direction. Nevertheless, this was already expected to happen, as it was forecasted by the REV analysis performed at Section 4.2.2. However, it is interesting to check that the most critical direction is actually the transverse one.

Table 4.4: Descriptive statistical analysis over the geometrical and macroscopic results on NSD1-NSD9. Thermal conductivity in $\mathrm{W\,m^{-1}\,K^{-1}}$.

	SSA $[\mathrm{m}^{-1}]$	SA $[\mathrm{m}^2]$	τ_X	τ_Y	τ_Z	κ_X	κ_Y	κ_Z
VAR.S	1.1e05	5.4e-15	1.1e-06	1.9e-06	1.6e-06	1.2e-04	1.1e-04	4.0e-05
STDEV.S	3.4e02	7.3e-08	1.0e-03	1.4e-03	1.2e-03	1.1e-02	1.0e-02	6.3e-03
AVG	3.1e05	6.79e-06	1.0793	1.0777	1.1314	0.4961	0.5088	0.0950
VAR%	1.08%	1.08%	0.10%	0.13%	0.11%	**2.22%**	**2.08%**	**6.67%**

A REV analysis was also carried out on these simulated cases. Again the results show that domains bigger than 1000^3 voxels would be required, which is above the computational power available[2]. In order to check the expected error at this size, the power functions of the REV analysis were obtained for each case, and the best and worst ones are plotted in Figure 4.3. From them, it can be extracted that a normalized standard deviation of 5 to 10 % shall be expected in the future results.

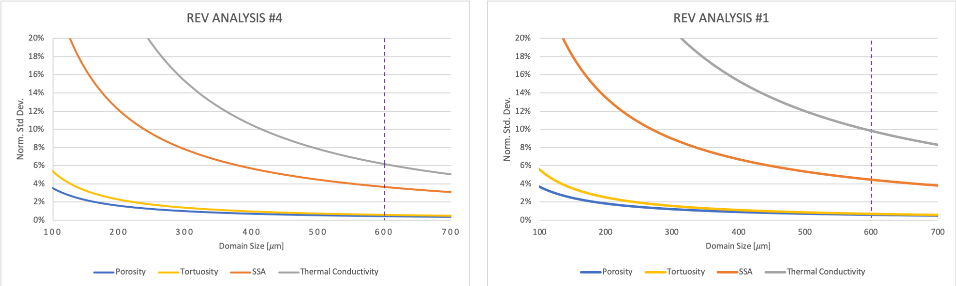

Figure 4.3: Extract of the REV analyses performed over the nine geometries (NSD1–NSD9). In particular, the fastest and the slowest converging cases.

To assess if the samples correspond to a normal distribution. A statistics analysis was carried to obtain measures of central tendency and variability, such as standard deviation, variance, kurtosis and skewness.

These last two values are the most representative to visualize how the data is distributed within the set of values. On the one hand, the skewness alludes the tendency of a distribution that determines its symmetry about the mean. On the other hand, the kurtosis is a measurement of the respective sharpness of the curve. In this way, a positive skewness denotes that the plot

---

[2] This was later improved by using the Hydra cluster

is extended towards the right side while a positive kurtosis represents that the distribution is more peaked than the normal distribution. Generally it is accepted that, for skewnesses in the range -0.5 to 0.5, the distribution assumed to be symmetric. However, values between -2 to 2 are usually considered acceptable in order to prove normal univariate distribution for both skewness and kurtosis [53].

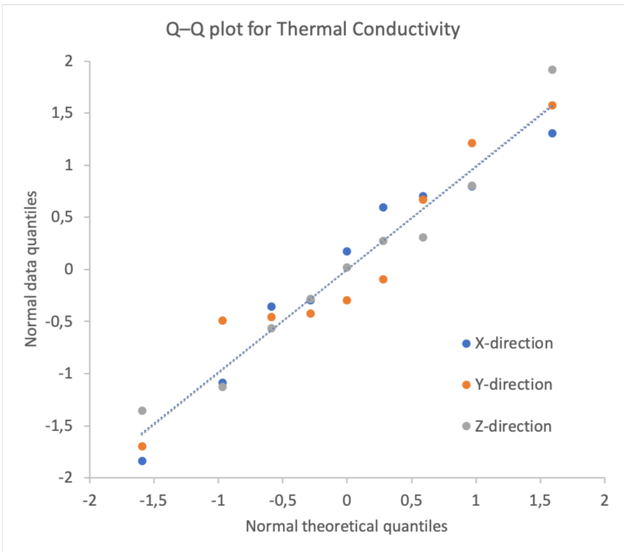

Figure 4.4: Q–Q plot of the normalized thermal conductivity versus a Normal distribution.

In this study, the skewness and the kurtosis remain under the -2 to 2 threshold for all the variables, and particularly for the thermal conductivity in the three directions, as it can be seen in Table 4.5. In fact, for X and Y-directions, it even lays into the definition given for symmetric distribution although just nine measurement can be taken into account.

In order to graphically verify these previous statements, a Q-Q (quantile-quantile) plot was represented for the three variables of interest in order to compare in a visual way the obtained results with the expected values for a normal distribution. In Figure 4.4 it can be double-checked that the data obtained complied with the expected for a theoretical standard normal distribution as the tendencies of the three properties follow the diagonal.

A last statistical analysis was done to check if the number of samples was large enough to be representative. A sample size calculation was undertaken with a 1% margins of error (MOE) with respect to the mean value, and 95% confidence levels ($\alpha^* = 0.05$), which correspond to a z-score such that the area to the right of $z_{\alpha^*/2} = z_{0.05/2}$ is equal to $\alpha^*/2$. Therefore $P(Z \geq$

$z_{\alpha^*/2}) = 0.025 \longrightarrow P(Z \leq z_{\alpha^*}) = 0.975$ and $z = 1.959964$ [3], which may be rounded to $z_{0.025} = 1.96$

$$n = \left(\frac{z_\alpha^* \cdot \sigma^*}{MOE} \right)^2 \tag{4.1}$$

Substituting the MOE, the sample standard deviation from Table 4.5 and $z_{0.025}$ into the sample size Equation (4.1), we are able to obtain that to comply with the selected characteristics, the sample size should have been of 20, 17 and 172 tests, respectively for X, Y and Z-directions. Nevertheless, if the confidence level was reduced to a 90%, just 14, 12 and 121 tests should have been performed.

Independently of the exact values of the sample sizes required, we can observe that the results obtained may be accepted, but the values for through-plane conductivity may lack some exactitude. Therefore, the uncertainty of the measured effective thermal conductivities was estimated to be within 10 %, due to the restriction in the size domain caused by the limited computational power.

Table 4.5: Descriptive statistics analysis output for the thermal conductivity.

k_X ***Analysis***		k_Y ***Analysis***		k_Z ***Analysis***	
Mean	0.4961	Mean	0.5099	Mean	0.0950
Std. Error	0.0044	Std. Error	0.0046	Std. Error	0.0021
Median	0.4980	Median	0.5066	Median	0.0952
Std. Dev.	0.0110	Std. Dev.	0.0111	Std. Dev.	0.0063
Samp. Var.	1.2e-04	Samp. Var.	1.1e-04	Samp. Var.	4.0e-05
Kurtosis	**-0.1521**		**-0.0333**		**0.5211**
Skewness	**-0.6820**		**0.1281**		**0.5568**
Range	0.0355	Range	0.0355	Range	0.0211
Min.	0.4676	Min.	0.4911	Min.	0.0864
Max.	0.5111	Max.	0.5266	Max.	0.1072
Sum	4.4651	Sum	4.5794	Sum	0.8554
Count	9	Count	9	Count	9
$\alpha^*_{0.95}$	0.009	$\alpha^*_{0.95}$	0.008	$\alpha^*_{0.95}$	0.005

---

[3] Obtained from Excel function `NormInv()`

4.3 Study on the influence of the microscopical properties

The developed parametric study was performed to check the influence of each microscopical variable over the effective conductivity of the geometries, and its main intention was to help in the development and understanding of an artificially-generated model which may represent a real porous material without the need of micro-CT.

As it was exposed in Section 4.1, the base model was generated attending to the reviewed characteristic of CALCARB® CBCF 18-2000, which also served for deciding the range of study of the variables of interest.

The first steps carried to perform this study was to generate 25 different geometries by taking 5 values of interest for the porosity 0.85, 0.87, 0.89, 0.91 and 0.92 [52], and other 5 for the orientation of the fibers 15, 18, 20, 22 and 25°. Moreover, two extra geometries were generated with a porosity of 0.85 and an angle of 10 and 30° to create an extended range for the verification of the trends.

With this step, a first analysis was done to measure the tortuosity of the material, by assuming a continuum regime. Knowing this, we can observe the results from the performed calculations in Figure 4.5, where it can be noticed that the porosity has an inverse effect in the tortuosity, as expressed by the Bruggeman relation [54], valid for a wide variety of materials if the pore phase is connected:

$$\tau = \epsilon^{0.5} \tag{4.2}$$

The orientation of the fibers in the Z direction has a different effect in the tortuosity depending on the direction analyzed. Clearly a wider distribution of fibers in Z direction increases tortuosity in the in-plane as the transport coefficients may be reduced due to an increase of the path that the fluid must walk to cross the tortuous medium. However, the inverse phenomena is observed in the Z-direction.

Also the SSA and the SA values were computed and compared to real data values to check for an extra validity of the model. However, it was acknowledged that while the SA is a very vague parameter to compare two structures, the SSA should have been compliant with the data obtained from literature, the manufacturer's brochure and experimental data provided by the VKI [55]. However, it was found out to be even several orders of magnitude lower. This can be attributed to the coastline paradox [56], as the higher the precision in your measurements is, the higher the distance measured will be. Therefore, as in PuMA theoretical cylinders of 1 µm are generated, if then is compared with surface area measurements performed

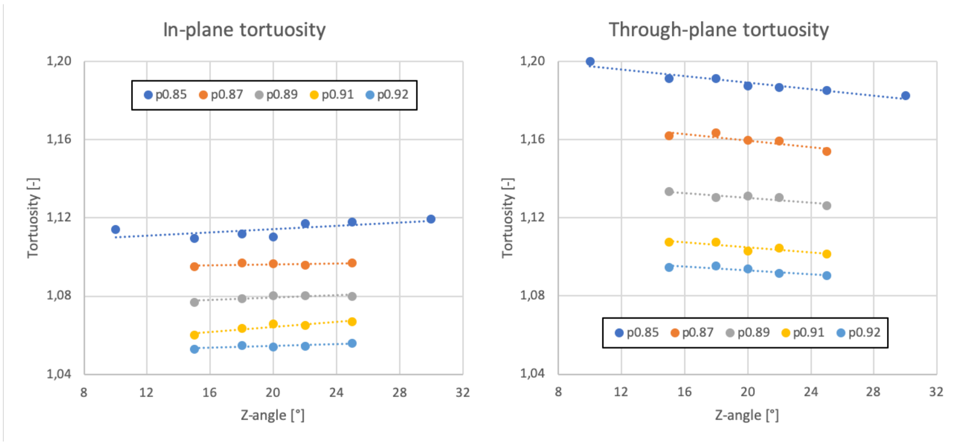

Figure 4.5: Parametric study for the tortuosity.

with the gas sorption method where pores down to 1.5 nm are taken into account, the comparison lacks cohesion.

Once the studies of the geometries where finished, a set of values for the gas conductivity was fixed 0, 0.01, 0.017 72, 0.025, 0.04 and 0.06. These values were agreed to be used based on the actual values of the environments in which usually LFA analyses are carried on and obtained through the use of specific databases included in the Mutation^{++} library [40].

An analysis was carried over each of the possible combinations and a 3x3 symmetric tensor was obtained for the effective thermal conductivity of each one of them, as the one in Equation (2.11).

The diagonal values were found to be predominant, attending that the generated geometries were designed as mostly orthotropic materials, meaning that in two of its main directions the conductivity is identical. Because of this reason, it was supposed that both the X and Y directions will perform similarly. This was proved afterwards that both directions, showed analogous results never exceeding a 2% variation, caused by the randomness of the geometry generation. The off-diagonal values were disregarded as they were always at least one order of magnitude smaller than those on the main diagonal.

From this matricial results, just two broad values were of main interest: the in-plane and the through-plane conductivities. The former was obtained by averaging the values of the X and Y directions, while the latter was represented only by the Z one.

As it can be already perceived for the first analysis with a vacuum environment with null thermal conductivity outside the fibers Figure 4.6, that porosity has a bigger influence over the effective variable, as compared with

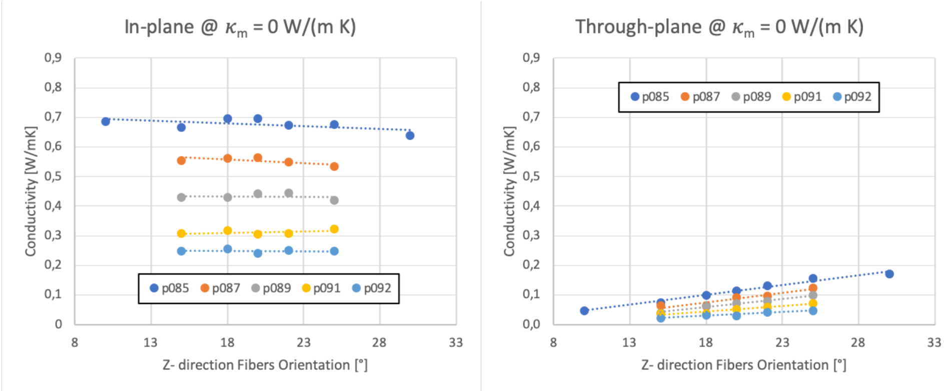
In-plane @ κ_m = 0 W/(m K)

Through-plane @ κ_m = 0 W/(m K)

Figure 4.6: Influence of porosity and fibers' orientation in Z direction on the effective conductivity. Case for a vacuum environment with null conductivity and $\kappa_{\mathrm{f}} = 12\,\mathrm{W\,m^{-1}\,K^{-1}}$.

the fibers' orientation in the in-plane section, while in the through plane it occurs the other way around.

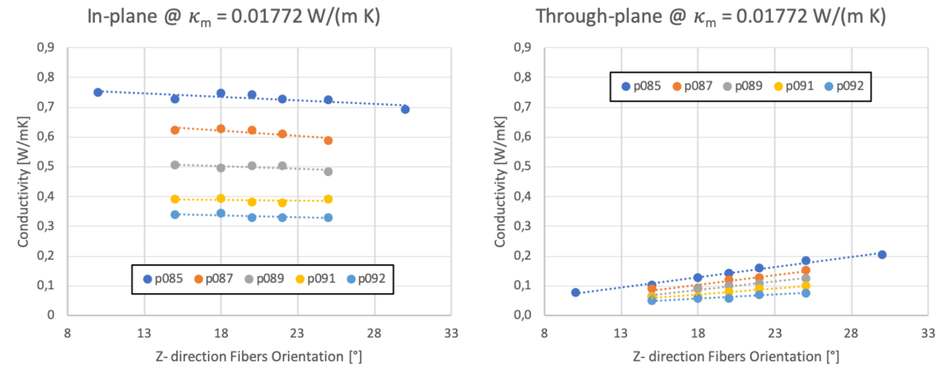
In-plane @ κ_m = 0.01772 W/(m K)

Through-plane @ κ_m = 0.01772 W/(m K)

Figure 4.7: Influence of porosity and fibers' orientation on the effective conductivity. Case for $\kappa_{\mathrm{m}} = 0.017\,72\,\mathrm{W\,m^{-1}\,K^{-1}}$ and $\kappa_{\mathrm{f}} = 12\,\mathrm{W\,m^{-1}\,K^{-1}}$.

This makes complete sense and complies with the initial surmises. As in the X-Y plane the distribution of fibers is homogeneous and they are distributed all over the domain, it is easy to understand why the influence of the intrinsic conductivities of the fibers is such. In that way, when increasing the porosity, the number of fibers, and thus the overall conductivity is notably reduced. On the other hand, in the Z-direction, as fibers are limited to a certain range, the influence of the intrinsic conductivity is also limited. Therefore the wider the range, the higher the conductivity in the Z direction through the fibers.

Also it should be noted that, as porosity increases, a reduction of the sensibility of the geometry to the orientation of the fibers may be obtained. This can be more specifically represented in the through-plane plots. Once again this can be understood as that a lower density of fibers must reduce the influence they have in the overall simulation.

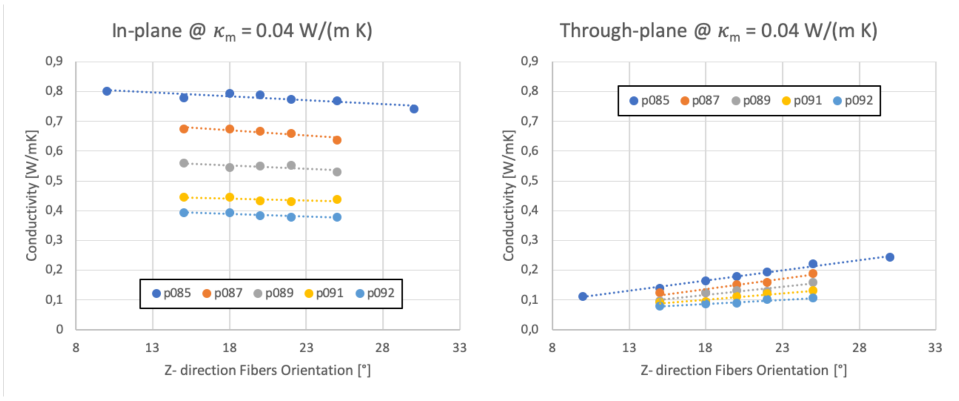

Figure 4.8: Influence of porosity and fibers' orientation on the effective conductivity. Case for $\kappa_\mathrm{m} = 0.04\,\mathrm{W\,m^{-1}\,K^{-1}}$ and $\kappa_\mathrm{f} = 12\,\mathrm{W\,m^{-1}\,K^{-1}}$.

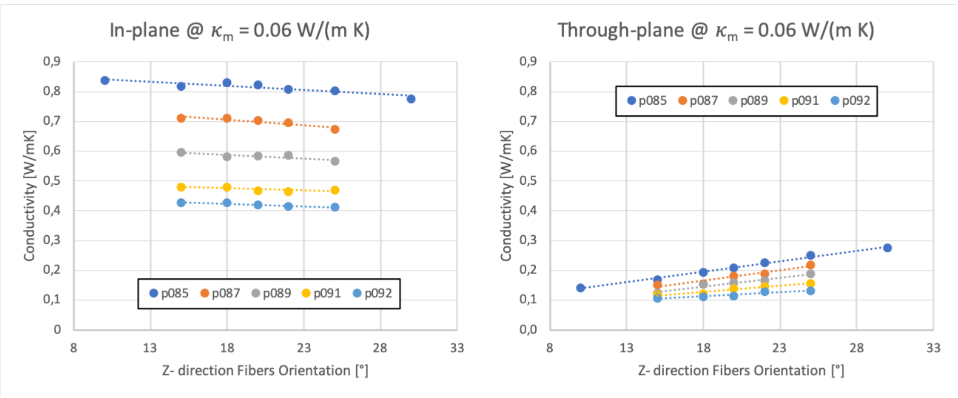

Figure 4.9: Influence of porosity and fibers' orientation on the effective conductivity. Case for $\kappa_\mathrm{m} = 0.06\,\mathrm{W\,m^{-1}\,K^{-1}}$ and $\kappa_\mathrm{f} = 12\,\mathrm{W\,m^{-1}\,K^{-1}}$.

As the medium's thermal conductivity increases through Figures 4.7 to 4.9, the same trends can be observed on the effective conductivity, as it was expected. Moreover, in Figure 4.10 it can be graphically observed this evolution. From This figure several conclusions may be drawn. First, it can be clearly verified how as the porosity (void volume fraction) increases, the influence of the gas is bigger. Moreover, it is thought that for higher values of κ_m, the growth stabilizes into a positive linear representation, rather than to an asymptote in the y-axis. In fact, in the through-plane analysis it can already be seen that tendency. Lastly, the influence of porosity over the conductive direction is proven to be much higher than on the insulating one, as previously explained.

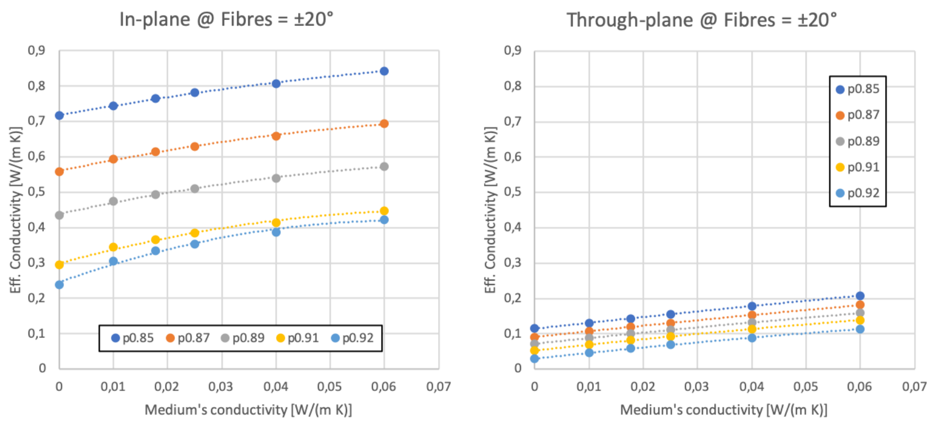

Figure 4.10: Influence of porosity and medium's conductivity on the effective conductivity. Case for a distribution of fibers with ±20° in Z-direction and $\kappa_\mathrm{f} = 12\,\mathrm{W\,m^{-1}\,K^{-1}}$.

This previous analysis it was done over a model with ±20° geometry. If we consider now the effect of the orientation of the fibers, as shown in Figure 4.11 (note the change of scale in the y-axis), an increment in the distribution of 10° has an important impact on the effective conductivity of the insulating direction, even doubling the value in some cases. This helps us realize how important is the fibers orientation in the material.

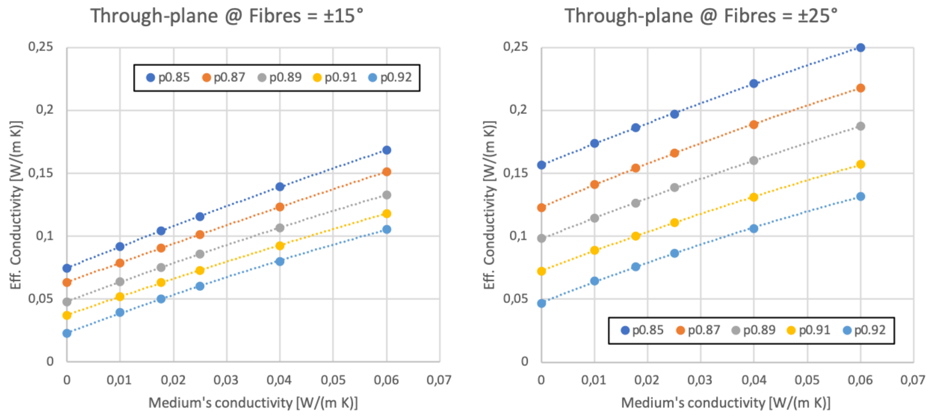

Figure 4.11: Influence of porosity and medium's conductivity on the effective conductivity. Case for a distribution of fibers with ±15° (left) and ±25° (right) in Z-direction.

However, the leading matter is the fibers' conductivity. A last analysis was carried to fully understand the importance of the selection of the material intrinsic conductivity. As it was shown in Figure 2.5, a rough approximation to the conductivity of the three different types of carbon fibers, are: $12\,\mathrm{W\,m^{-1}\,K^{-1}}$ for the TC2 (rayon-based), $40\,\mathrm{W\,m^{-1}\,K^{-1}}$ for the P33 (PAN-based) and $200\,\mathrm{W\,m^{-1}\,K^{-1}}$ for the P100 (pitch-based). Given the same geometry, the effective conductivity was computed for the different types of fibers (Fig. 4.12). This shows importance of choosing the adequate type of carbon fiber, as roughly has a linear 1:1 dependency one on the other. An increment of 15 times in the fiber's conductivity entails an equal increase in the effective parameter, almost independently of the porosity of the sample.

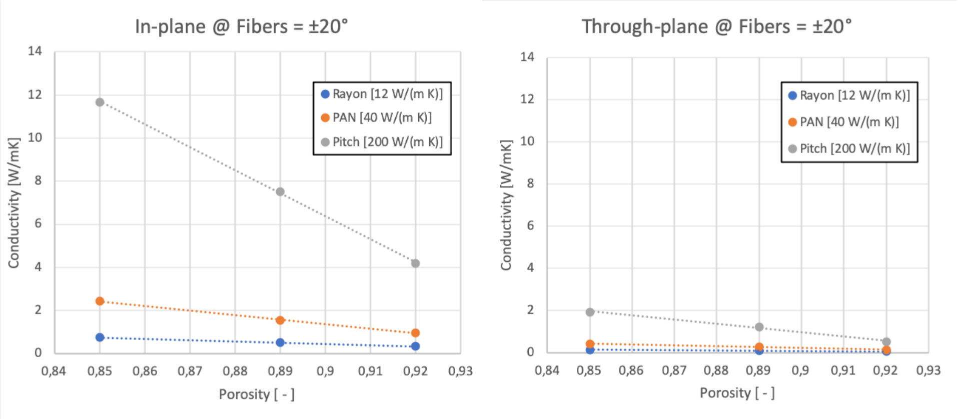

Figure 4.12: Influence of porosity and fibers' origin on the effective conductivity. Case for a distribution of fibers with ±20° in Z-direction and $\kappa_\mathrm{m} = 0.017\,72\,\mathrm{W\,m^{-1}\,K^{-1}}$

Chapter 5

Development of simulated CALCARB® CBCF 18-2000

The development of the aforementioned model and parametric study will be now compared against real experimental data with a double purpose. On the one hand this will help to validate the synthetic model. On the other hand, it will help to understand the technical documentation issued by the furnisher. Moreover, the model will also serve to reproduce and partly explain the experimental results obtained through LFA in the context of the AblaNTIS experimental test campaign carried by the VKI.

5.1 Comparison with experimental data

It was elemental to perform a comparative analysis with the real material in order to prove or discard the validity of the model created. However, the currently available experimental data of CALCARB® CBCF 18–2000 [34, 38] is limited to the effective conductivity of the material, so it was not possible to verify the tortuosity or other interesting properties.

The effective conductivity was presented as a function of temperature and the medium in which the material was tested, giving the values for vacuum, nitrogen and argon. The literature data available does not report the direction (in-plane or through-plane) in which the measurements were performed. Nevertheless, as it will be discussed afterwards, with the developed model we were able to retrieve this information.

The comparison was performed in two steps: i) constant intrinsic conductivity of the fibers of $12\,\mathrm{W\,m^{-1}\,K^{-1}}$, ii) intrinsic conductivity as a function of temperature as in [36, 57]. In both cases the conductivity of the medium was a function of temperature and composition computed with Mutation^{++}.

Even if in the former case the assumption done was really simplistic, and the latter was thought to be more accurate, extra assumptions may apply for both cases. On the one hand, the artificially-generated geometry must be assumed to be similar enough to the real samples. On the other hand, as in PuMA it is not possible to include temperature as a variable, the input properties must be chosen to represent it.

Case i): Constant intrinsic conductivity of the fibers

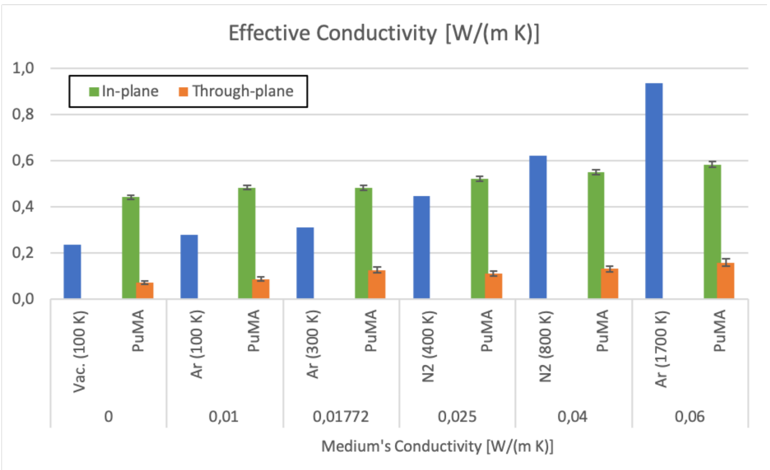

Figure 5.1: Comparison of experimental vs. computationally-obtained values for the effective thermal conductivity of CALCARB® CBCF 18–2000 as a function of the conductivity of the medium. Error bars displayed from the results of Section 4.2.3.

In Figure 5.1 it can be seen that neither of the cases analyzed in PuMA was compliant with the expected values. However, it was noted that, while in the in-plane the difference with the experimental values increased linearly from -80% to +40%, in the through-plane it just increased from a 70 to an 80%. This lead to think that the problem was caused by the constant conductivity assumption, as the effective conductivity in-plane direction (i.e. stronger influence of the fibers) was almost constant, while in the through-plane direction (i.e. where the gas has a bigger influence) the correlation was more effective, but between 4 and 6 times smaller.

Case ii): Temperature dependent intrinsic conductivity of the fibers

The temperature-dependent intrinsic conductivity of the fibers was obtained from [36, 57] by digitizing the reported figures [58]. However, due to the low resolution of those figures, the reliability of the digitized data was rather low. Therefore, it was decided to verify the consistency of these data by computing the conductivity from the heat capacity and the thermal diffusivity (Eq. (2.10)) also reported in the aforementioned references.

It must be also mentioned that the density of the material was at every moment assumed constant, so the thermal expansion was assumed negligible and no variation was accounted for the char remainders.

In this case temperatures of 400, 1000, 1600 and 2000 K were used as they were directly provided by the manufacturer, so avoiding additional uncertainty brought by the extrapolation. This way, an intrinsic conductivity of the fibers of 8, 12, 20 and $26\,\mathrm{W\,m^{-1}\,K^{-1}}$ was obtained respectively for each temperature [36].

The comparison was first carried out in the vacuum environment, where one variable falls from the equation. Then a value available on the documentation was retrieved and the conductivity of the carbon fibers was double-checked through the digitization procedure, plus the calculation of thermal conductivity through the thermal diffusivity.

With this new set up the results obtained were more compliant with the reference values. As it can be seen in Figure 5.2, the in-plane effective conductivity simulated correlates with the experimental data of CALCARB®. Moreover, it can be seen how the conductivity of the material given by the manufacturer [34, 38] is indeed provided for the conductive (or in-plane) direction.

In Table 5.1, a comparison in percentage is shown, between the experimental value and the numerically-obtained one. First it was checked in a vacuum environment, how the correlation is effective in both directions, being the difference $\sim 5\%$ for the in-plane direction, and $\sim 80\%$ for the through-plane one. When the case was repeated in Argon, the results showed similar outputs. Lastly, the computations were done including nitrogen as medium. The divergence in this analysis may be caused by the nitridation phenomena. This exothermic reaction ($\mathrm{C_s + N \rightleftharpoons CN}$) occurs between the solid carbon from the fibers and atomic nitrogen. As temperature increases, the dissociation of nitrogen becomes more relevant starting at temperatures larger than 700 °C. This reaction has been supposed to be affecting the results by increasing the measured (apparent) heat conductivity, thus inducing a systematic error in the measurement. However, this should be verified with further study.

These analyses validate the carbon fiber preform model generated in PuMA, which correctly represents the values of a real material. It should be noted that an accurate computation of the effective conductivity of the carbon fiber preform only required a minimal number of inputs, namely:

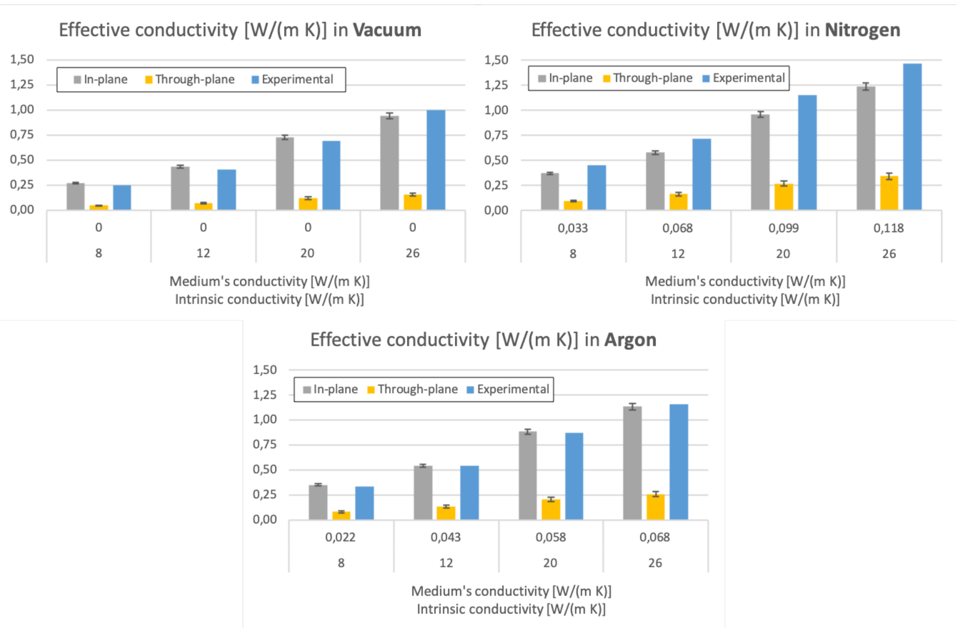

Figure 5.2: Comparison of experimental vs. computationally-obtained values for the effective thermal conductivity of CALCARB® CBCF 18–2000 as a function of the conductivity of the medium and the fibers. Error bars displayed from the results of Section 4.2.3.

conductivity of the fibers and the medium, and geometrical parameters of the material including the porosity or the fiber's characteristics.

This is a very interesting approach since we could consider a numerical design of materials with a certain optimization criterion in mind.

5.2 Simulations of LFA results

In the context of the Ablative-material Numerical-Test International Series (AblaNTIS) project of the European Space Agency (ESA), developed by the VKI, the main expected outcome is a numerical test-case booklet on the response of carbon-phenolic ablators to plasma flow [33]. As part of this project, As part of this project experimental thermal diffusivity measurements were performed at Julich by means of LFA.

In these analyses, the effective thermal conductivity of pre-charred[1] ZURAM®, were characterized for the in-plane and through-plane directions, during a whole process to heat the material up to the limit temperature of

---

[1] Thermal treatment applied to ablative materials to decompose the polymeric matrix and simulate the fibers after being exposed to relatively high temperatures.

Table 5.1: Comparison of experimental vs. computationally-obtained values for the effective thermal conductivity $\mathrm{W\,m^{-1}\,K^{-1}}$ of Calcarb® CBCF 18–2000, for the in-plane and through-plane cases.

Temp. [K]	κ_f	κ_m	In-plane	Δ%	Thru-plane	Δ%	Exptl.
				Vacuum			
400	8	0	0.27	8%	0.05	-81%	0.25
1000	12	0	0.44	6%	0.07	-83%	0.41
1600	20	0	0.73	5%	0.12	-83%	0.69
2000	26	0	0.94	-6%	0.16	-84%	1.00
				Nitrogen			
400	8	0.03	0.39	-13%	0.11	-76%	0.45
1000	12	0.07	0.58	-19%	0.17	-77%	0.72
1600	20	0.10	0.96	-16%	0.27	-77%	1.15
2000	26	0.19	1.24	-16%	0.34	-77%	1.47
				Argon			
400	8	0.02	0.35	5%	0.08	-76%	0.33
1000	12	0.04	0.55	1%	0.14	-75%	0.54
1600	20	0.06	0.88	2%	0.21	-76%	0.87
2000	26	0.07	1.14	-2%	0.26	-78%	1.16

2800 °C and cool down to ambient temperature again, in order to test how these properties were modified. Preliminary tests showed a non-negligible increase (up to 400% for some cases) of the measured thermal diffusivity of the material during the cooling phase with respect to the measured diffusivity measured at the same temperatures during the heating phase, as it can be seen in Figure 5.3.

At first, this was an unexpected result, but literature search attributed this change to a process called graphitization[59]. In carbon fibers this phenomenon occurs approximately around 2500 to 3000 K [60], through which graphitic structures are generated from an amorphous carbon, resulting in a better alignment of the atoms along the fiber axis.

The manufacturers of carbon fibers typically pre-treat their materials at relatively high temperatures to (presumably) avoid this effect. This is the case for the carbon preform of study CBCF-2000, which is pretreated at 2000 °C. This can be seen in Figure 5.3 where the cases in which the maximum temperature was below the pretreatment temperature (blue and orange curves), the conductivity remained unchanged during the cooldown. However, in the cases where this limit was passed, an increase of the con-

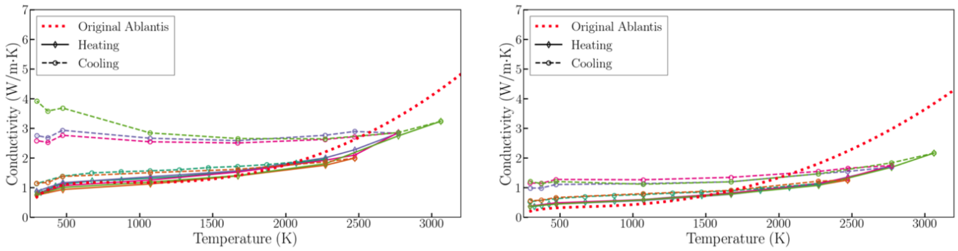

Figure 5.3: In-plane (left) and through-plane (right) thermal conductivity of charred ZURAM® based on LFA tests (i.e. thermal diffusivity) and Eq. (2.10) [33].

ductivity was observed in the cooldown measurements. This is particularly important for atmospheric re-entry, where such high temperatures are usually encountered.

Since the current hypothesis for this change in effective thermal conductivity is that the carbon atoms have been re-arranged in the fibers, we consider that this re-arrangement has increased the intrinsic conductivity of fibers, which consequently increased the effective one. Therefore, the objective of this section is to compute the intrinsic conductivity of the graphitized fibers given the effective one (inverse modeling).

Here we assumed the pre-charred ZURAM® material to be equal to the model generated for CALCARB® CBCF 18–2000. This hypothesis seems reasonable since the pre-charring process consists of pyrolyizing the resin, leading to a relatively small quantity of char; part of this char falls from the material, while another part gets attached to the fibers. The quantification of the change in porosity due to this was computed to be 0.02 [33].

Table 5.2: Effective conductivity for pre-charred ZURAM®, at 200 °C

Eff. therm. conductivity	[W/(m K)]	Pre-test	Post-test
AblaNTIS	In-plane	0.86	3.17
	Through-plane	0.44	1.27

The case analyzed was at 200 °C for fibers pretreated up to 2800 °C since it was the case with the highest difference between pre- and post-test. Data was once again double checked by the digitization of Figure 5.3, and the calculation of thermal conductivity through Equation (2.10) and the thermal diffusivity obtained from the experimental analyses. These values are shown at Table 5.2.

These LFA experiments were carried out using Helium as media, so through Mutation^{++}, its conductivity was obtained to be $\kappa_{\mathrm{He}\ @200\,^{\circ}\mathrm{C}} =$

0.212 $\mathrm{W\,m^{-1}\,K^{-1}}$ at 473.15 K.

The methodology to verify the variation in the intrinsic conductivity of the fibers was undertaken in two steps: i) reproduce the pre-test results with the same model and intrinsic conductivity used during the whole development of this work (12 $\mathrm{W\,m^{-1}\,K^{-1}}$), ii) through a "manual bisection method", find the intrinsic parameter which gives the same effective conductivity as the experimental value.

However it was later realized that the geometry used may not be representative of the characteristic of the sample. Indeed, when generating the synthetic model the orientation of the fibers for CALCARB® CBCF 18-2000 were not available, they were supposed equivalent to other precursors of similar characteristics (FiberForm). Now, it has been observed that an angle of ±30 to 35° fits better the characteristics of pre-charred ZURAM®.

Table 5.3: Computed effective conductivity for different artificially-generated geometries. Error is computed with respect to experimental values from Table 5.2

Fibers' orientation	Conduct. [W/(m K)]	Pre-test	Error %	Post-test	Error %
±20°	In-plane	0.87	-1%	3.14	1%
	Through-plane	0.39	16%	0.75	41%
	Intrinsic	12		57	
±25°	In-plane	0.88	-2%	3.21	-1%
	Through-plane	0.42	4%	0.94	26%
	Intrinsic	12		60	
±30°	In-plane	0.86	0%	3.20	-1%
	Through-plane	0.45	-3%	1.17	8%
	Intrinsic	12		62	
±35°	In-plane	0.86	0%	3.20	-1%
	Through-plane	0.47	-7%	1.24	2%
	Intrinsic	12		62	

As it can be seen in Figure 5.4 (note the change of scale in Y axis), when the in-plane conductivity is equalized with the experimental values, in the pre-test results a barely-comparable difference is found due to the reduced values, but in the post-test it can be clearly checked how for the original model, the values are not compliant. As we increase the angular distribution, the analyses start matching. Therefore, it was agreed on the validity of a case with 30 to 35° orientation of the fibers in the Z direction.

In this specific case, it can be seen in Table 5.3 that the required intrinsic conductivity obtained should have a value of 62 $\mathrm{W\,m^{-1}\,K^{-1}}$ which is around 5 times the value performed before the test, so the increase is not negligible.

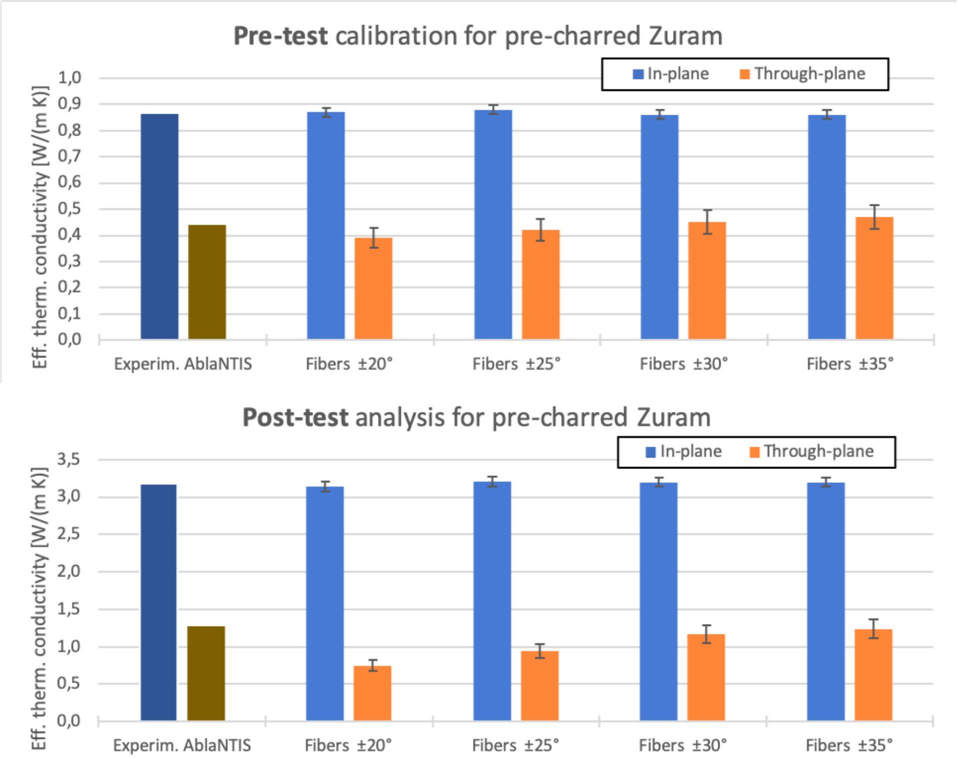

Figure 5.4: Comparison of experimental and numerical results for in- and through-plane conductivities of pre-charred ZURAM® on different geometries. Error bars displayed from the results of section 4.2.3.

Chapter 6

Conclusions and future work

The developments of this project can be divided into three main parts. First, a synthetic model was generated and the influence of its properties was evaluated through a parametric study. Second, a comparison with real experimental data was performed in order to verify the model created. Last, a simulation of the effects obtained through LFA was implemented to improve the understanding of porous ablative materials.

6.1 Recapitulation

As a general conclusion, this thesis demonstrates that through the use of numerical software such as PuMA, an accurate characterization and modeling of porous materials can be achieved. This can be used to extract useful macroscopic properties from micro-scale simulations. The specific conclusions of each part are presented below.

Conclusions on the synthetic model analysis

A digital reproduction of the main characteristics of CALCARB® CBCF 18–2000 was developed in PuMA software from a minimal number of inputs from literature. A statistical analysis was performed over this geometry to test its validity. From it the following conclusions were drawn:

- Through the REV analysis implemented in PuMA it was obtained that a synthetic material with the characteristics of typical porous CF ablators requires domains greater than 1000^3 voxels.
- Even though the domain size generated was restricted because of computational limitations, it was proven that the expected error was smaller

than a 2% on every parameter except for through-plane conductivity, which had a 10% error bound.

Afterwards, a parametric study was designed to evaluate the influence of the properties of interest. Through it, expected trends were proven:

- Increasing the porosity has an important diminishing effect on the effective conductivity, regardless of the direction, as the environment is less conductive than the fibers.
- A broader distribution of fibers in Z direction, increases the conductivity through-plane two times as much as it reduces it in-plane.
- For the design of spacecraft heat shields, the appropriate choice of the CF precursor is key, as effective conductivity has an almost-linear dependence (1:1) on the intrinsic conductivity (keeping the remaining variables constant). This supports the fact that aerospace industry chooses rayon fibers over other types.

Conclusions on the verification with experimental data

The model generated in the first part was then compared with the experimental data of CALCARB®.

- When taking into account the temperature dependency on all the model variables in PuMA, a great agreement between the artificially-generated geometry and the real sample is obtained, within a certain degree of incertitude attributed to the limited size of the model.
- From this correlation it could be understood that the scalar value provided in the technical documentation by the manufacturer for the conductivity of the material corresponds to the conductive direction. The insulating one shows around 5 times lower conductivity.

The validation of the computational model is a very interesting conclusion, since it allows to consider numerical designs of materials in order to faithfully represent real properties, seeking a certain optimization criterion for desired applications.

Conclusions on the study of LFA results

Lastly, the numerical model was used to understand the variation of the intrinsic conductivity of pre-charred ZURAM®, when exposed to high temperatures.

- The geometry of the model (fibers' distribution in Z-direction) had to be slightly adapted to faithfully represent the experiment.
- When exposed to temperatures up to 2800 °C, the effective conductivity of the material is modified due to an increase of ~ 5 times the intrinsic conductivity of its fibers.

This increase on the effective thermal conductivity should be taken into account in future missions in which carbon/phenolic ablators are planned to be re-used.

6.2 Future work

The development of this thesis leaves some room for further developments:

- Verification of properties and run of a REV analysis over a bigger domain.
- Comparison of artificial models with the analysis of microtomographies from real materials.
- Study of the effect of a nitrogen environment on the conductivity of carbon fiber materials.
- Development of a numerical solver to represent LFA analysis through the PuMA software, simulating the laser shot in one surface and observing the change in temperature on the other side.

In addition, slightly further away from this project, it would be interesting to evaluate the effect of the change on the conductivity due to the graphitization of the fibers on the re-usability of ablative TPS. The idea of re-using them has been proposed in the past from companies such as SpaceX, but this graphitization effect has not been reported in the literature of TPS design, so its impact may be unknown for the design.

Bibliography

[1] S. M. Johnson, Thermal Protection Materials and Systems: Past, Present, and Future, NASA Ames Research Center (2013) 73.

[2] D. A. Day, Shuttle thermal protection system (TPS) (Jul 2002).
URL `https://www.centennialofflight.net/essay/Evolution_of_Technology/TPS/Tech41.htm`

[3] B. Laub, E. Venkatapathy, Thermal protection system technology and facility needs for demanding future planetary missions, ESA Publications Division 544 (2004) 239–247.

[4] R. H. Goddard, Report concerning further developments in space travel (Sep 2012).
URL `https://siarchives.si.edu/history/featured-topics/stories/march-1920-report-concerning-further-developments-space-travel`

[5] B. D. Dunn, Materials and Processes, Springer International Publishing, Cham, 2016. `doi:10.1007/978-3-319-23362-8`.
URL `http://link.springer.com/10.1007/978-3-319-23362-8`

[6] K. Triantou, K. Mergia, S. Florez, B. Perez, J. Barcena, W. Rotärmel, G. Pinaud, W. Fischer, Thermo-mechanical performance of an ablative/ceramic composite hybrid thermal protection structure for re-entry applications, Composites Part B: Engineering 82 (2015) 159 – 165. `doi:https://doi.org/10.1016/j.compositesb.2015.07.020`.
URL `http://www.sciencedirect.com/science/article/pii/S1359836815004485`

[7] T. Reimer, C. Zuber, J. Rieser, T. Rothermel, Determination of the Mechanical Properties of the Lightweight Ablative Material Zuram, in: N. P. Bansal, R. H. Castro, M. Jenkins, A. Bandyopadhyay, S. Bose, A. Bhalla, J. P. Singh, M. M. Mahmoud, G. Pickrell, S. Johnson (Eds.), Ceramic Transactions Series, John Wiley & Sons, Inc., Hoboken, NJ, USA, 2018, pp. 311–326. `doi:10.1002/9781119423829.ch28`.
URL `http://doi.wiley.com/10.1002/9781119423829.ch28`

[8] M. Rallini, M. Natali, L. Torre, Chapter 14 - an introduction to ablative materials and high-temperature testing protocols, in: Q.-L. Yan, G.-Q. He, P.-J. Liu, M. Gozin (Eds.), Nanomaterials in Rocket Propulsion Systems, Micro and Nano Technologies, Elsevier, 2019, pp. 529 – 549. `doi:https://doi.org/10.1016/B978-0-12-813908-0.00014-9`.
URL `http://www.sciencedirect.com/science/article/pii/B9780128139080000149`

[9] G. Pulci, J. Tirillò, F. Marra, F. Fossati, C. Bartuli, T. Valente, Carbon–phenolic ablative materials for re-entry space vehicles: Manufacturing and properties, Composites Part A: Applied Science and Manufacturing 41 (10) (2010) 1483–1490. `doi:10.1016/j.compositesa.2010.06.010`.
URL `https://linkinghub.elsevier.com/retrieve/pii/S1359835X10001776`

[10] J. Lachaud, J. Scoggins, T. Magin, M. Meyer, N. Mansour, A generic local thermal equilibrium model for porous reactive materials submitted to high temperatures, International Journal of Heat and Mass Transfer 108, Par B (2017) 1406–1417. `doi:10.1016/j.ijheatmasstransfer.2016.11.067`.
URL `https://linkinghub.elsevier.com/retrieve/pii/S0017931016312480`

[11] K. Raed, U. Gross, Modeling of Influence of Gas Atmosphere and Pore-Size Distribution on the Effective Thermal Conductivity of Knudsen and Non-Knudsen Porous Materials, Int J Thermophys 30 (4) (2009) 1343–1356. `doi:10.1007/s10765-009-0600-8`.
URL `http://link.springer.com/10.1007/s10765-009-0600-8`

[12] N. N. Mansour, Multi-scale modeling of low-density carbon-phenolic ablators, NASA Peer Committee (2018) 83.

[13] J. M. Thornton, F. Semeraro, S. J. Visser, A. Borner, J. C. Ferguson, F. Panerai, N. N. Mansour, Microscale analysis of spacecraft heat shields, Tech. rep., NASA Ames Research Center (November 2019).

[14] A. Wiegmann, A. Zemitis, EJ-HEAT: A Fast Explicit Jump Harmonic Aver- aging Solver for the Effective Heat Conductivity of Composite Materials, Berichte des Fraunhofer ITWM (2006) 37.

[15] N. B. Carrigy, L. M. Pant, S. Mitra, M. Secanell, Knudsen diffusivity and permeability of PEMFC microporous coated gas diffusion layers for different polytetrafluoroethylene loadings, Journal of The Electrochemical Society 160 (2) (2012) F81–F89. `doi:10.1149/2.036302jes`.
URL `https://doi.org/10.1149%2F2.036302jes`

[16] S. Antman, J. Marsden, L. Sirovich (Eds.), Microflows and Nanoflows, Vol. 29 of Interdisciplinary Applied Mathematics, Springer-Verlag, New York, 2005. `doi:10.1007/0-387-28676-4`.
URL `http://link.springer.com/10.1007/0-387-28676-4`

[17] J. Rouquerol, D. Avnir, C. W. Fairbridge, D. H. Everett, J. M. Haynes, N. Pernicone, J. D. F. Ramsay, K. S. W. Sing, K. K. Unger, Recommendations for the characterization of porous solids (Technical Report), Pure and Applied Chemistry 66 (8) (1994) 1739–1758. `doi:10.1351/pac199466081739`.
URL `http://www.degruyter.com/view/j/pac.1994.66.issue-8/pac199466081739/pac199466081739.xml`

[18] IUPAC, micropore in catalysis, in: A. D. McNaught, A. Wilkinson (Eds.), IUPAC Compendium of Chemical Terminology, 2nd Edition, IUPAC, Blackwell Scientific Publications, Oxford (1997), 2009, p. 585. `doi:10.1351/goldbook.M03906`.
URL `http://goldbook.iupac.org/M03906.html`

[19] G. M. Nielson, Dual Marching Tetrahedra: Contouring in the Tetrahedronal Environment, in: Advances in Visual Computing, Vol. 5358, Springer Berlin Heidelberg, Berlin, Heidelberg, 2008, pp. 183–194, series Title: Lecture Notes in Computer Science. `doi:10.1007/978-3-540-89639-5_18`.
URL `http://link.springer.com/10.1007/978-3-540-89639-5_18`

[20] W. E. Lorensen, H. E. Cline, Marching cubes: A high resolution 3d surface construction algorithm, SIGGRAPH Comput. Graph. 21 (4) (1987) 163–169. `doi:10.1145/37402.37422`.
URL `https://doi.org/10.1145/37402.37422`

[21] J. C. Ferguson, F. Panerai, A. Borner, N. N. Mansour, M. Field, Porous Materials Analysis (PuMA) Version 2., NASA/TM (2016) 130.

[22] G. M. Nielson, Dual marching tetrahedra: Contouring in the tetrahedronal environment, in: in Advances in Visual Computing, Springer, 2008, pp. 183–194.

[23] D. Mugler, R. Scott, Fast fourier transform method for partial differential equations, case study: The 2-d diffusion equation, Computers & Mathematics with Applications 16 (3) (1988) 221 – 228. `doi:https://doi.org/10.1016/0898-1221(88)90182-4`.
URL `http://www.sciencedirect.com/science/article/pii/0898122188901824`

[24] J. C. Ferguson, A. Borner, F. Panerai, N. N. Mansour, Particle methods for tortuosity factors in porous media, Ablation WS (2018) 30.

[25] S. Cooper, D. Eastwood, J. Gelb, G. Damblanc, D. Brett, R. Bradley, P. Withers, P. Lee, A. Marquis, N. Brandon, P. Shearing, Image based modelling of microstructural heterogeneity in lifepo4 electrodes for li-ion batteries, Journal of Power Sources 247 (2014) 1033 – 1039. `doi:https://doi.org/10.1016/j.jpowsour.2013.04.156`.
URL `http://www.sciencedirect.com/science/article/pii/S0378775313007763`

[26] C. Gommes, A. Bons, S. Blacher, J. Dunsmuir, A. Tsou, Practical methods for measuring the tortuosity of porous materials from binary or gray-tone tomographic reconstructions, AIChE Journal 55 (08 2009). `doi:10.1002/aic.11812`.

[27] J. C. Ferguson, F. Panerai, A. Borner, N. N. Mansour, PuMA: the Porous Microstructure Analysis software, SoftwareX 7 (2018) 81–87. `doi:10.1016/j.softx.2018.03.001`.
URL `https://linkinghub.elsevier.com/retrieve/pii/S2352711018300281`

[28] J. A. R. Borges, L. F. Pires, A. Belmont Pereira, Computed Tomography to Estimate the Representative Elementary Area for Soil Porosity Measurements, The Scientific World Journal 2012 (2012) 1–10. `doi:10.1100/2012/526380`.
URL `http://www.hindawi.com/journals/tswj/2012/526380/`

[29] A. S. Pagan, C. Zuber, B. Massuti-Ballester, G. Herdrich, H. Hald, S. Fasoulas, The Ablation Performance and Dynamics of the Heat Shield Material ZURAM, 31st International Symposium on Space Technology and Science (2017) 11.

[30] B. Helber, F. Torres Herrador, V. Leroy, A. Turchi, O. Chazot, T. E. Magin, Experiments of the ZURAM carbon-phenolic ablator for test case definition and material code validation., in: 9th Ablation Workshop, Bozeman, Montana USA, 2017, p. 34.

[31] F. Torres-Herrador, T. E. Magin, B. Helber, A. Turchi, A. Fagnani, O. Chazot, Material properties and ablation performance of the ZURAM ablator for material response code validation, in: 10th Ablation Workshop, Burlington, Vermont USA, 2018, p. 34.

[32] F. Torres-Herrador, B. Helber, A. Turchi, S. Gorugantu, K. M. Van Geem, O. Chazot, T. Magin, J. Blondeau, Characterization of the thermal degradation of the carbon-phenolic materials: an experimental effort on the ZURAM ablator., in: International Conference on Flight vehicles, Aerothermodynamics and Re-entry Missions and Engineering, ESA Publications Division, Monopoli, Italy, 2019, p. 8.

[33] A. Turchi, B. Helber, F. Torres Herrador, T. Magin, L. Chipperfield, F. Pascon, T. Eekelen, H. Ritter, Ablative-material numerical-test international series (AblaNTIS): An experimental/numerical effort to support the validation of material thermal-response tools., in: International Conference on Flight vehicles, Aerothermodynamics and Re-entry Missions and Engineering (FAR) 2019, 2019, p. 9.

[34] Mersen, Properties of Calcarb ®, rigid carbon insulation CBCF 15-2000, Tech. rep., Mersen, accessed February 2020 (February 2009).
URL `https://www.mersen.com/sites/default/files/publications-media/3-gs-calcarb-grade-cbcf-15-2000-mersen.pdf`

[35] P. Bhatt, A. Goe, Carbon Fibres: Production, Properties and Potential Use, Material Science Research India 14 (1) (2017) 52–57. `doi:10.13005/msri/140109`.
URL `http://www.materialsciencejournal.org/vol14no1/carbon-fibres-production-properties-and-potential-use/`

[36] C. Pradere, J. Batsale, J. Goyhénèche, R. Pailler, S. Dilhaire, Thermal properties of carbon fibers at very high temperature, Carbon 47 (3) (2009) 737–743. `doi:10.1016/j.carbon.2008.11.015`.
URL `https://linkinghub.elsevier.com/retrieve/pii/S0008622308006015`

[37] S. R. Bakshi, D. Lahiri, A. Agarwal, Carbon nanotube reinforced metal matrix composites - a review, International Materials Reviews 55 (1) (2010) 41–64. `doi:10.1179/095066009X12572530170543`.
URL `http://www.tandfonline.com/doi/full/10.1179/095066009X12572530170543`

[38] Mersen, Calcarb rigid carbon insulation, Tech. rep., Mersen, accesed March 2020 (February 2013).
URL `https://www.graphite-eng.com/uploads/downloads/calcarb_brochure.pdf`

[39] B. Helber, Material response characterization of low-density ablators in atmospheric entry plasmas, Ph.D. thesis, von Karman Institute for Fluid Dynamics, Belgium (2016).

[40] J. Scoggins, T. Magin, Development of mutation++: Multicomponent thermodynamic and transport properties for ionized plasmas written in `C++`, in: 11th AIAA/ASME Joint Thermophysics and Heat Transfer Conference, 2014, p. 15. `doi:10.2514/6.2014-2966`.

[41] J. D. B. O'Sullivan, J. Behnsen, T. Starborg, A. S. MacDonald, A. T. Phythian-Adams, K. J. Else, S. M. Cruickshank, P. J. Withers, X-ray micro-computed tomography: an emerging opportunity in parasite

imaging, Parasitology 145 (7) (2018) 848–854. `doi:10.1017/S0031182017002074`.
URL `https://www.cambridge.org/core/product/identifier/S0031182017002074/type/journal_article`

[42] T. Baba, A. Ono, Improvement of the laser flash method to reduce uncertainty in thermal diffusivity measurements, Measurement Science and Technology 12 (2001) 2046.

[43] W. J. Parker, R. J. Jenkins, C. P. Butler, G. L. Abbott, Flash Method of Determining Thermal Diffusivity, Heat Capacity, and Thermal Conductivity, Journal of Applied Physics 32 (9) (1961) 1679–1684.

[44] H. S. Carslaw, J. C. Jaeger, Conduction of Heat in Solids, Clarendon Press ; Oxford University Press, 1959.

[45] Y.-H. Zhao, Z.-K. Wu, S.-L. Bai, Thermal resistance measurement of 3D graphene foam/polymer composite by laser flash analysis, International Journal of Heat and Mass Transfer 101 (2016) 470–475. `doi:10.1016/j.ijheatmasstransfer.2016.05.068`.
URL `https://linkinghub.elsevier.com/retrieve/pii/S0017931015313296`

[46] J. Lachaud, G. Vignoles, A brownian motion technique to simulate gasification and its application to c/c composite ablation, Computational Materials Science 44 (4) (2009) 1034 – 1041. `doi:https://doi.org/10.1016/j.commatsci.2008.07.015`.
URL `http://www.sciencedirect.com/science/article/pii/S0927025608003522`

[47] V. Rutka, Z. Li, An explicit jump immersed interface method for two-phase Navier–Stokes equations with interfaces, Computer Methods in Applied Mechanics and Engineering 197 (25-28) (2008) 2317–2328. `doi:10.1016/j.cma.2007.12.016`.
URL `https://linkinghub.elsevier.com/retrieve/pii/S0045782508000030`

[48] J. Crank, The mathematics of diffusion, 2nd Edition, Clarendon Press, Oxford, [Eng], 1975.

[49] J. M. Zalc, S. C. Reyes, E. Iglesia, The effects of diffusion mechanism and void structure on transport rates and tortuosity factors in complex porous structures, Chemical Engineering Science 59 (14) (2004) 2947 – 2960. `doi:https://doi.org/10.1016/j.ces.2004.04.028`.
URL `http://www.sciencedirect.com/science/article/pii/S0009250904002623`

[50] M. Espinoza-Andaluz, M. Andersson, B. Sundén, Computational time and domain size analysis of porous media flows using the lattice Boltzmann method, Computers & Mathematics with Applications 74 (1) (2017) 26–34. `doi:10.1016/j.camwa.2016.12.001`.
URL `https://linkinghub.elsevier.com/retrieve/pii/S0898122116306721`

[51] J. Ahrens, B. Geveci, C. Law, 36 - ParaView: An end-user tool for large-data visualization, in: C. D. Hansen, C. R. Johnson (Eds.), Visualization Handbook, Butterworth-Heinemann, Burlington, 2005, pp. 717 – 731. `doi:https://doi.org/10.1016/B978-012387582-2/50038-1`.
URL `http://www.sciencedirect.com/science/article/pii/B9780123875822500381`

[52] F. Panerai, J. D. White, T. J. Cochell, O. M. Schroeder, N. N. Mansour, M. J. Wright, A. Martin, Experimental measurements of the permeability of fibrous carbon at high-temperature, International Journal of Heat and Mass Transfer 101 (2016) 267 – 273. `doi:https://doi.org/10.1016/j.ijheatmasstransfer.2016.05.016`.
URL `http://www.sciencedirect.com/science/article/pii/S0017931016307207`

[53] D. George, P. Mallery, SPSS for Windows step by step: a simple guide and reference, 17.0 update, 10th Edition, Allyn & Bacon, Boston, 2010, oCLC: ocn318421024.

[54] L. Pisani, Simple Expression for the Tortuosity of Porous Media, Transp Porous Med 88 (2) (2011) 193–203. `doi:10.1007/s11242-011-9734-9`.
URL `http://link.springer.com/10.1007/s11242-011-9734-9`

[55] F. Torres-Herrador, Sample B - Microactive, Tech. rep., Micromeritics, internal summary report (2019).

[56] R. Stoa, The Coastline Paradox, SSRN Journal (2019). `doi:10.2139/ssrn.3445756`.
URL `https://www.ssrn.com/abstract=3445756`

[57] J. Wang, B. Song, X. Zhang, Y. Song, G. Wu, Simultaneous Measurements of Thermal Properties of Individual Carbon Fibers, Int J Thermophys 32 (5) (2011) 974–983. `doi:10.1007/s10765-011-0961-7`.
URL `http://link.springer.com/10.1007/s10765-011-0961-7`

[58] A. Rohatgi, Webplotdigitizer v.4.2 (April 2017).
URL `https://automeris.io/WebPlotDigitizer`

[59] M. B. Vázquez-Santos, E. Geissler, K. László, J.-N. Rouzaud, A. Martínez-Alonso, J. M. Tascón, Comparative XRD, Raman, and

TEM Study on Graphitization of PBO-Derived Carbon Fibers, The Journal of Physical Chemistry C 116 (1) (2012) 257–268. `doi:10/b345b5`.
URL `https://doi.org/10.1021/jp2084499`

[60] H. Marsh, F. Rodríguez-Reinoso, Chapter 9 - production and reference material, in: H. Marsh, F. Rodríguez-Reinoso (Eds.), Activated Carbon, Elsevier Science Ltd, Oxford, 2006, pp. 454 – 508. `doi:https://doi.org/10.1016/B978-008044463-5/50023-6`.
URL `http://www.sciencedirect.com/science/article/pii/B9780080444635500236`